ARTICLES
https://doi.org/10.1038/s41593-021-00827-3
nature neuroscience

Check for updates

# Gain of toxic function by long-term AAV9-mediated SMN overexpression in the sensorimotor circuit

Meaghan Van Alstyne[1,2,3], Ivan Tattoli[1,2], Nicolas Delestrée[1,2,3], Yocelyn Recinos[1,4,5], Eileen Workman[1,2], Lamya S. Shihabuddin[6], Chaolin Zhang[1,4,5], George Z. Mentis[1,2,3] and Livio Pellizzoni[1,2,3] ✉

**The neurodegenerative disease spinal muscular atrophy (SMA) is caused by deficiency in the survival motor neuron (SMN) protein. Currently approved SMA treatments aim to restore SMN, but the potential for SMN expression beyond physiological levels is a unique feature of adeno-associated virus serotype 9 (AAV9)-SMN gene therapy. Here, we show that long-term AAV9-mediated SMN overexpression in mouse models induces dose-dependent, late-onset motor dysfunction associated with loss of proprioceptive synapses and neurodegeneration. Mechanistically, aggregation of overexpressed SMN in the cytoplasm of motor circuit neurons sequesters components of small nuclear ribonucleoproteins, leading to splicing dysregulation and widespread transcriptome abnormalities with prominent signatures of neuroinflammation and the innate immune response. Thus, long-term SMN overexpression interferes with RNA regulation and triggers SMA-like pathogenic events through toxic gain-of-function mechanisms. These unanticipated, SMN-dependent and neuron-specific liabilities warrant caution on the long-term safety of treating individuals with SMA with AAV9-SMN and the risks of uncontrolled protein expression by gene therapy.**

SMA is an autosomal recessive neurodegenerative disorder characterized by motor neuron loss and skeletal muscle atrophy, which represents the leading genetic cause of infant death[1,2]. Individuals with SMA have homozygous deletions or mutations in the survival motor neuron 1 *(SMN1)* gene with retention of the hypomorphic *SMN2* gene that produces low levels of SMN due to defective splicing of a critical exon[3,4], the skipping of which leads to an unstable rapidly degraded form of the protein[1,2]. The disease is classified into four clinical groups (types 1, 2, 3 and 4) based on time of onset and severity that inversely correlate with *SMN2* copy number and SMN protein levels[1,2].

Therapeutic approaches for all SMA types have mainly focused on increasing SMN expression through antisense oligonucleotides (ASOs)[5,6] or small molecules[7,8] that correct *SMN2* splicing, as well as SMN replacement by gene therapy with AAV9 vectors[9–12], all of which have demonstrated efficacy in preclinical animal models and human clinical trials. Importantly, repeated intrathecal injections of an *SMN2* splicing-modifying ASO (nusinersen (Spinraza))[13–15] and gene therapy via a single intravenous administration of AAV9-SMN (onasemnogene abeparvovec (Zolgensma))[16,17] are currently used for treatment of the disease. Recently, the US Food and Drug Administration (FDA) has also approved the use of an orally bioavailable compound that promotes *SMN2* splicing (risdiplam (Evrysdi)) for SMA therapy[18]. All three drugs have shown a favorable safety and efficacy profile, but in different populations of individuals with SMA [19].

At a time when SMN-inducing therapies with different mechanisms of action are given to individuals with SMA, it is critical to compare and contrast their benefits and potential liabilities. Unlike approaches aimed at correcting splicing of endogenous *SMN2* and therefore subject to an intrinsic limit of SMN induction, the potential for SMN expression beyond physiological levels is uniquely associated with AAV9-SMN gene therapy. Furthermore, the biology of SMN overexpression and the long-term safety profile of AAV9-SMN are largely unknown.

To date, FDA-approved gene therapy by intravenous administration of AAV9-SMN in individuals under 2 years of age has shown early clinical benefit in infants with type 1 SMA who have the most severe form of the disease without major adverse events beyond an acute but transient elevation in liver transaminases that is controlled pharmacologically[16]. Although only a few years have passed since the first individuals were treated, follow-up studies up to 2 years from initial AAV9-SMN treatment did not show signs of decline in functional gain[17]. Nevertheless, evidence is accumulating that AAV9-SMN can cause neuronal toxicity in animal models and its potential relevance to individuals with SMA is beginning to be recognized even if clinical manifestations may take many years. A recent study reported that systemic administration of an AAV9-like SMN vector induced toxicity in large animal models[20], which included dorsal root ganglia (DRG) pathology and inflammation leading to severe ataxia in piglets but no overt motor deficits in nonhuman primates. Similar neuropathological findings in DRG were independently reported following intrathecal delivery of the FDA-approved AAV9-SMN vector in nonhuman primates[21,22]. Since intrathecal injection of AAV9-SMN was being pursued in a clinical trial as a candidate therapeutic approach for treatment of individuals with milder SMA [21], these indications raised sufficient safety concerns for the FDA to put the trial on partial clinical hold. Altogether, these findings prompted an urgent need to determine the full spectrum of potential toxicities of AAV9-SMN

[1]Center for Motor Neuron Biology and Disease, Columbia University, New York, NY, USA. [2]Department of Pathology and Cell Biology, Columbia University, New York, NY, USA. [3]Department of Neurology, Columbia University, New York, NY, USA. [4]Department of Systems Biology, Columbia University, New York, NY, USA. [5]Department of Biochemistry and Molecular Biophysics, Columbia University, New York, NY, USA. [6]Neuroscience Therapeutic Area, Sanofi, Framingham, MA, USA. ✉e-mail: lp2284@cumc.columbia.edu

and their underlying mechanisms, which are currently unknown. Importantly, it has been proposed that toxicity may be driven by injection of high doses of the AAV vector itself through mechanisms unrelated to either the capsid type or the transgene[20]. In contrast, the possibility that overexpression of the therapeutic gene product (that is, SMN) could be toxic to neurons in the long term has never been considered. Here we sought to address these outstanding questions in mouse models.

## Results

**AAV9-mediated SMN overexpression induces sensorimotor deficits in mouse models.** We found strong early phenotypic improvement of SMNΔ7 SMA mice following a one-time intracerebroventricular delivery of a therapeutic dose of $5\times10^{10}$ vector genomes per gram (vg $g^{-1}$) of self-complementary AAV9-SMN at postnatal day (P) 0 (Fig. 1). AAV9-SMN-treated SMA mice showed enhanced motor function and increased weight gain and survival relative to AAV9-GFP-treated SMA mice (Fig. 1a–c). These results are consistent with previous preclinical studies in this model that used the same vector in which SMN expression is driven by the ubiquitous β-glucuronidase (GUSB) promoter[10,23] as well as other promoters[9,11,12]. While different from the hybrid cytomegalovirus enhancer/chicken β-actin (CBA) promoter present in the FDA-approved AAV9-SMN vector for SMA gene therapy[9,16], GUSB is a weaker promoter than CBA for AAV-mediated gene expression in vivo[24]. Surprisingly, we found that SMA mice treated with AAV9-SMN developed the neurological phenotype of hind-limb clasping, determined as retraction of the limbs to the torso and clenching of the digits[25], at around 4 months of age (Fig. 1d,e). To investigate this without confounding factors of the SMA phenotype, we analyzed wild-type (WT) mice that were untreated or injected with either AAV9-GFP or AAV9-SMN and found that AAV9-SMN specifically induced hind-limb clasping characterized by earlier onset with increasing doses (Fig. 1f,g and Supplementary Video 1). At doses where hind-limb clasping occurred, the phenotype was fully penetrant in all treated animals and grew progressively more pronounced following initial onset. Moreover, the lowest dose of AAV9-SMN that we tested did not induce hind-limb clasping, but was previously shown to be suboptimal for correction of the SMA phenotype[23]. Some premature deaths and reduced weight gain also occurred in WT mice treated with the highest dose of AAV9-SMN (Fig. 1h,i). Further behavioral analysis using rotarod and inverted-grid assays showed dose-dependent, progressive impairment in motor performance of WT mice treated with AAV9-SMN relative to both uninjected and AAV9-GFP-treated controls (Fig. 1j,k), which led to hind-limb paralysis in mice treated with the highest dose (Supplementary Video 2). These results demonstrate that long-term AAV9-mediated SMN overexpression induces dose-dependent, late-onset motor deficits in mouse models.

**AAV9-mediated SMN overexpression causes synaptic loss and neurodegeneration.** The hind-limb clasping phenotype in mice is associated with compromised information about limb and joint position, altered reflexes, or the improper integration of sensory and motor information including dysfunction of proprioceptive neurons[25]. Therefore, we performed electrophysiological studies to investigate the muscle (M) response and the H-reflex by recording electromyography activity in vivo from the interosseous muscle of the hind paw after sciatic nerve stimulation (Extended Data Fig. 1a–c). This analysis can reveal differences in proprioceptive synaptic function (H-reflex) and motor neuron function (M-response), with the H/M ratio determining whether either response is more affected. There were no alterations in the amplitude of the M-response even after repetitive nerve stimulation at high frequencies (Extended Data Fig. 1d,g), indicating normal synaptic transmission at the neuromuscular junction (NMJ). In contrast, the amplitude of the H-reflex and H/M ratio were reduced in AAV9-SMN-treated mice relative to controls (Extended Data Fig. 1e,f), consistent with dysfunction of proprioceptive synapses.

To investigate the cellular basis of these SMN-dependent defects, we quantified the number of proprioceptive synapses on lumbar L5 motor neurons innervating muscles involved in the clasping phenotype. We found a strong, dose-dependent reduction of vesicular glutamate transporter 1 (VGluT1)-positive synapses on somata and proximal dendrites of motor neurons in AAV9-SMN-injected WT mice at P150, which worsened with aging (Fig. 2a–c), while cholinergic C-boutons were unaffected (Extended Data Fig. 2d,e). We further analyzed effects of SMN overexpression on the survival of proprioceptive neurons from L5 DRG and L5 lateral motor column (LMC) motor neurons in WT mice. We found that AAV9-SMN caused late-onset, dose-dependent loss of proprioceptive neurons (Fig. 3a,b), as well as shrinkage of soma size and reduced survival of motor neurons together with early signs of NMJ innervation deficits at P300 (Fig. 3c–e and Extended Data Fig. 2). Thus, AAV9-mediated SMN overexpression induces selective deafferentation of motor neurons and late-onset neurodegeneration in WT mice.

We then investigated whether AAV9-SMN had similar late-onset effects in the sensorimotor circuit of SMA mice, which display motor neuron death, NMJ denervation and loss of proprioceptive inputs as disease-specific deficits induced by SMN deficiency[2]. AAV9-SMN significantly improved all of these disease-related deficits when assessed at P11 relative to AAV9-GFP-treated SMA mice (Fig. 2d,e and Extended Data Fig. 3a–e). Specifically, the number of VGluT1$^+$ proprioceptive synapses onto motor neuron somata was decreased by 70% in SMA mice injected with AAV9-GFP relative to control SMNΔ7 WT mice and fully rescued by treatment with AAV9-SMN at P11 (Fig. 2d,e), consistent with early correction of sensorimotor circuit deficits[26,27]. Remarkably, however, the same proprioceptive synapses showed a dramatic reduction by P190 in AAV9-SMN-treated SMA mice (Fig. 2d,e). These findings indicate that AAV9-SMN treatment in SMA mice promotes early rescue of the disease-linked loss of proprioceptive synapses onto SMA motor neurons[27,28], but this correction is followed by a late-onset loss of the same synapses due to gain of toxic function of long-term SMN overexpression. Similarly, the soma size of motor neurons that was strongly reduced in GFP-treated SMA mice was fully rescued by AAV9-SMN at P11, with an SMN-dependent reduction again apparent at P190 (Extended Data Fig. 3c). In contrast, AAV9-SMN-mediated correction of NMJ innervation and motor neuron survival that are severely affected in SMA mice at P11 did not change over time and no loss of proprioceptive neurons was observed at P190 (Extended Data Fig. 3d–f). Note that AAV9-GFP-treated SMA mice did not survive past 14 d of age (Fig. 1c) and therefore could not be analyzed at P190; later time points could also not be analyzed in SMA mice treated with AAV9-SMN due to their relatively limited survival extension (Fig. 1c). Collectively, these results reveal that selective deafferentation of motor neurons compounded by late-onset neurodegenerative processes are common features of sensorimotor toxicity induced by AAV9-SMN across mouse models.

**AAV9-SMN drives overexpression and cytoplasmic aggregation of SMN in neurons.** To gain insight into mechanisms of AAV9-SMN toxicity, we first assessed transgene expression over time. Immunohistochemistry showed high transduction and sustained GFP expression in motor neurons and proprioceptive neurons of WT mice at P11 and P300 (Fig. 4a). Further, the percentage of transduction of these neurons at P300 is comparable to levels we previously reported at P11 (Extended Data Fig. 4a,b)[28,29]. In contrast to neurons, GFP expression in the liver was high and widespread at P11, but nearly absent by P300 (Fig. 4a). These findings were

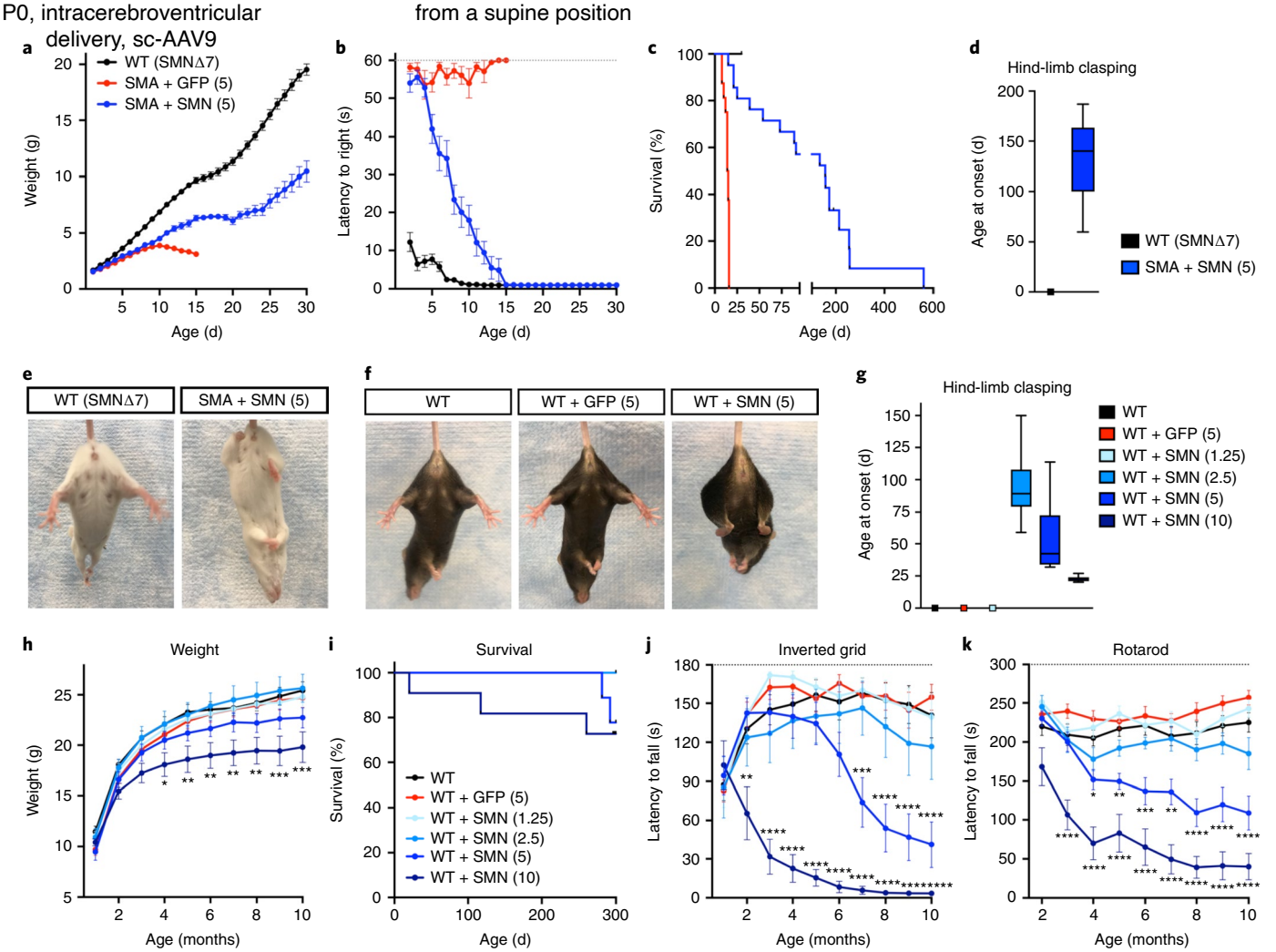


**Fig. 1 | Long-term AAV9-mediated SMN overexpression induces sensorimotor toxicity in WT and SMA mice. a–c**, Weight gain (**a**), righting time (**b**) and survival (**c**) of WT (SMNΔ7) mice ($n=17$) and SMA mice injected with $5\times10^{10}$ vg g$^{-1}$ (5) of AAV9-GFP ($n=16$) or AAV9-SMN ($n=21$) at P0. Data represent the mean and s.e.m. Weight gain: $P<0.0001$, $F_{2712}=718.3$, two-way ANOVA. Righting time: $P<0.0001$, $F_{2661}=1242$, two-way ANOVA. Survival: $P<0.0001$, d.f. $=2$, $\chi^2=54.58$, two-tailed Mantel–Cox log-rank test. **d**, Time of onset of hind-limb clasping in AAV9-SMN (5)-treated SMA mice ($n=5$). The box-and-whiskers graph shows the median, interquartile range, minimum and maximum. WT (SMNΔ7) mice ($n=5$) do not display hind-limb clasping. **e**, Hind-limb clasping phenotype observed in SMA mice treated with AAV9-SMN (5) at P190. **f**, Hind-limb clasping phenotype in AAV9-SMN-injected WT mice compared to uninjected and AAV9-GFP-treated controls at P300. **g**, Time of onset of hind-limb clasping in WT mice injected with $2.5\times10^{10}$ vg g$^{-1}$ (2.5) ($n=7$), $5\times10^{10}$ vg g$^{-1}$ (5) ($n=10$) and $1\times10^{11}$ vg g$^{-1}$ (10) ($n=10$) of AAV-SMN. Uninjected WT mice ($n=17$) and WT mice treated with $5\times10^{10}$ vg g$^{-1}$ (5) of AAV9-GFP ($n=16$) or $1.25\times10^{10}$ vg g$^{-1}$ (1.25) of AAV-SMN ($n=10$) did not display hind-limb clasping. The box-and-whiskers graph shows the median, interquartile range and minimum and maximum values. **h**, Weight gain of uninjected and AAV9-injected WT mice from the same groups as in **g**. Data represent the mean and s.e.m. Statistics were performed with two-way ANOVA ($P<0.0001$, $F_{5609}=26.28$) and Tukey's multiple-comparisons test results between WT and WT + SMN (10): week 4, $P=0.0147$; week 5, $P=0.0030$; week 6, $P=0.0051$; week 7, $P=0.0073$; week 8, $P=0.0033$; week 9, $P=0.0005$; week 10, $P=0.0005$). $^*P<0.05$; $^{**}P<0.01$; $^{***}P<0.001$. **i**, Survival analysis of uninjected and AAV9-injected WT mice from the same groups as in **g**. $P=0.0179$, d.f. $=5$, $\chi^2=13.66$, two-tailed Mantel–Cox log-rank test. **j**, Latency to fall on the inverted-grid test from the same groups as in **g**. Data represent the mean and s.e.m. Statistics were performed with two-way ANOVA ($P<0.0001$, $F_{5609}=105.9$) and Tukey's multiple-comparisons test results between WT and WT + SMN (5): week 7, $P=0.0003$; week 8–10, $P<0.0001$; or WT and WT + SMN (10): week 2, $P=0.0062$; week 3–10, $P<0.0001$. $^{**}P<0.01$; $^{***}P<0.001$; $^{****}P<0.0001$. **k**, Performance of WT mice from the same groups as in **g** on the rotarod assay. Data represent the mean and s.e.m. Statistics were performed with two-way ANOVA ($P<0.0001$, $F_{5543}=169.9$) and Tukey's multiple-comparisons test results between WT and WT + SMN (5): week 4, $P=0.0443$; week 5, $P=0.0035$; week 6, $P=0.0002$; week 7, $P=0.0034$; week 8–10, $P<0.0001$; or WT and WT + SMN (10): week 3–10, $P<0.0001$. $^*P<0.05$; $^{**}P<0.01$; $^{***}P<0.001$; $^{****}P<0.0001$.

confirmed by analysis of viral-mediated GFP and human SMN expression at the RNA and protein levels in both WT and SMA mice (Fig. 4b–e and Extended Data Figs. 4 and 5). Western blot analysis of WT mice injected with AAV9-SMN demonstrated overexpression of SMN above endogenous levels found in spinal cord (~two-fold) and liver (~20-fold) from uninjected and AAV9-GFP-injected controls at P11 (Fig. 4b–e), which was maintained in the spinal cord but lost in the liver at P300 (Fig. 4b–e). Overall similar results were found in SMA mice (Extended Data Fig. 5), although the levels of SMN overexpression appeared lower than those in WT mice. This may reflect differences in genetic background (FVB versus C57BL/6J) and/or phenotype (normal versus SMA) of the mouse

The hind-limb clasping phenotype in mice is associated with compromised information about limb and joint position, altered reflexes or the improper integration of sensory and motor information including dysfunction of proprioceptive neurons



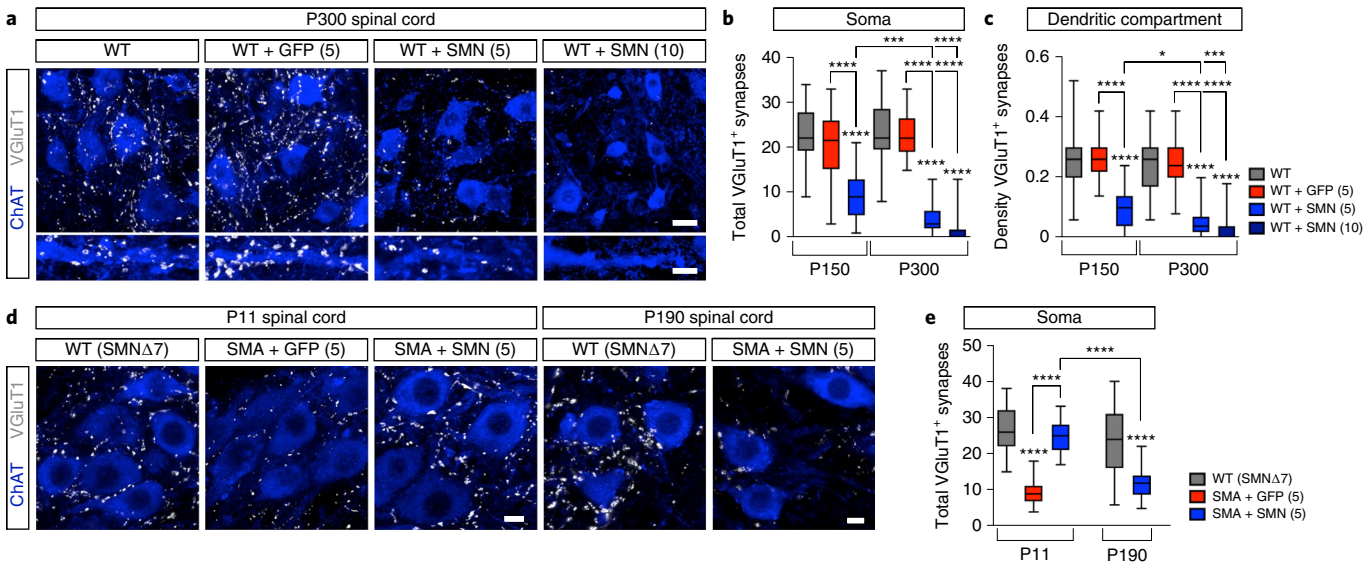


**Fig. 2 | AAV9-SMN induces late-onset deafferentation of motor neurons in WT and SMA mice. a**, Choline acetyltransferase (ChAT) and VGluT1 immunostaining of L5 LMC motor neuron somata and dendrites from uninjected, AAV9-GFP (5) and AAV9-SMN (5 and 10)-injected WT mice at P300. Scale bar, 25 µm. Dendrites scale bar, 10 µm. **b**, Total number of VGluT1+ synapses on L5 LMC motor neuron somata at P150 and P300 from the same groups as in **a**. The box-and-whiskers graph shows the median, interquartile range and minimum and maximum values from the following number of neurons and animals per group at P150 (WT, $n=39$ neurons, $n=3$ animals; WT + GFP (5), $n=36$ neurons, $n=3$ animals; WT + SMN (5), $n=57$ neurons, $n=3$ animals) and P300 (WT, $n=41$ neurons, $n=3$ animals; WT + GFP (5), $n=41$ neurons, $n=3$ animals; WT + SMN (5), $n=39$ neurons, $n=3$ animals; WT + SMN (10), $n=36$ neurons, $n=4$ animals). Statistics were performed with one-way ANOVA with Tukey's post hoc test. ****$P<0.0001$; ***$P<0.001$. WT P150 versus SMN (5) P150: $P<0.0001$, $q=16.96$, d.f. = 283; GFP (5) P150 versus SMN (5) P150: $P<0.0001$, $q=13.81$, d.f. = 283; WT P300 versus SMN (5) P300: $P<0.0001$, $q=22.64$, d.f. = 283; WT P300 versus SMN (10) P300: $P<0.0001$, $q=25.65$, d.f. = 283; GFP (5) P300 versus SMN (5) P300: $P<0.0001$, $q=22.14$, d.f. = 283; GFP (5) P300 versus SMN (10) P300: $P<0.0001$, $q=25.16$, d.f. = 283; SMN (5) P150 versus SMN (5) P300: $P=0.001$, $q=6.581$, d.f. = 283; SMN (5) P150 versus SMN (10) P300: $P<0.0001$, $q=10.16$, d.f. = 283. **c**, Density of VGluT1+ synapses on L5 LMC motor neuron proximal dendrites (number of synapses divided by the dendritic length up to 50 µm from soma) at P150 and P300 from the same groups as in **a**. The box-and-whiskers graph shows the median, interquartile range and minimum and maximum values from the following number of dendrites and animals per group at P150 (WT, $n=35$ dendrites, $n=3$ animals; WT + GFP (5), $n=26$ dendrites, $n=3$ animals; WT + SMN (5), $n=33$ dendrites, $n=3$ animals) and P300 (WT, $n=36$ dendrites, $n=3$ animals; WT + GFP (5), $n=31$ dendrites, $n=3$ animals; WT + SMN (5), $n=37$ dendrites, $n=3$ animals; WT + SMN (10), $n=35$ dendrites, $n=4$ animals). Statistics were performed with one-way ANOVA with Tukey's post hoc test. ****$P<0.0001$; ***$P<0.001$; *$P<0.05$. WT P150 versus SMN (5) P150: $P<0.0001$, $q=12.90$, d.f. = 226; GFP (5) P150 versus SMN (5) P150: $P<0.0001$, $q=12.77$, d.f. = 226; WT P300 versus SMN (5) P300: $P<0.0001$, $q=16.95$, d.f. = 226; WT P300 versus SMN (10) P300: $P<0.0001$, $q=18.55$, d.f. = 226; GFP (5) P300 versus SMN (5) P300: $P<0.0001$, $q=16.74$, d.f. = 226; GFP (5) P300 versus SMN (10) P300: $P<0.0001$, $q=18.30$, d.f. = 226; SMN (5) P150 versus SMN (5) P300: $P=0.0261$, $q=4.523$, d.f. = 226; SMN (5) P150 versus SMN (10) P300: $P=0.0003$, $q=6.258$, d.f. = 226. **d**, ChAT and VGluT1 immunostaining of L2 spinal segments from WT (SMNΔ7) mice and SMA mice treated with AAV9-GFP (5) or AAV9-SMN (5) at the indicated times. Scale bar, 10 µm. **e**, Total number of VGluT1+ synapses on L2 motor neuron somata from the same groups as in **d**. The box-and-whiskers graph shows the median, interquartile range and minimum and maximum values from the following number of neurons from $n=3$ animals per group at P11 (WT (SMNΔ7), $n=31$ neurons; SMA + GFP (5), $n=38$ neurons; SMA + SMN (5), $n=34$ neurons) and P190 (WT (SMNΔ7), $n=27$ neurons; SMA + SMN (5), $n=30$ neurons). Statistics were performed with one-way ANOVA with Tukey's post hoc test. ****$P<0.0001$. WT (SMNΔ7) P11 versus SMA + GFP (5) P11: $P<0.0001$, $q=16.76$, d.f. = 155; SMA + GFP (5) P11 versus SMA + SMN (5) P11: $P<0.0001$, $q=15.09$, d.f. = 155; WT (SMNΔ7) P190 versus SMA + SMN (5) P190: $P<0.0001$, $q=10.34$, d.f. = 155; SMA + SMN (5) P11 versus SMA + SMN (5) P190: $P<0.0001$, $q=12.51$, d.f. = 155.

models and also account for the delayed onset of the hind-limb clasping phenotype induced by AVV9-SMN in SMA compared with WT mice (Fig. 1d,g).

Western blot data largely underestimate the actual degree of SMN overexpression specifically in transduced cells such as motor neurons due to differences of AAV9 tropism in distinct tissues. While AAV9-GFP showed that most DRG neurons and liver cells are transduced (Fig. 4a), viral tropism in the spinal cord is much more selective, leading to efficient targeting and strong expression in ~70% of motor neurons but few other spinal cells (Fig. 4a and Extended Data Fig. 4a)[28,29]. The tissue-specific AAV9 transduction profile likely accounts for differences in the total levels of full-length human SMN mRNA measured by quantitative PCR with reverse transcription (RT–qPCR) in the spinal cord, liver and DRG of AAV9-SMN-treated SMA mice at P11 that are ~40-, ~700- and ~2,500-fold higher, respectively, than those in AAV9-GFP-injected SMA mice and uninjected WT littermates in which full-length SMN is expressed from two copies of the *SMN2* gene (Extended Data Fig. 5a–c). Even considering that *SMN2* genes express only ~10% of full-length SMN mRNA relative to a normal *SMN1* allele[1,2], these data provide direct evidence for vast overexpression of SMN well beyond normal physiological levels in motor circuit neurons transduced by AAV9-SMN.

We next sought to analyze the subcellular distribution of SMN expressed by AAV9 over time. The expected localization of endogenous SMN throughout the cytoplasm and in nuclear bodies called 'gems' was observed in motor neurons and proprioceptive neurons from uninjected and AAV-GFP-injected mice (Fig. 5a,b and Extended Data Fig. 6a,c). In stark contrast, motor neurons and proprioceptive neurons from WT and SMA mice injected with AAV9-SMN showed accumulation of SMN in cytoplasmic aggregates that grow larger over time (Fig. 5a,b and Extended Data

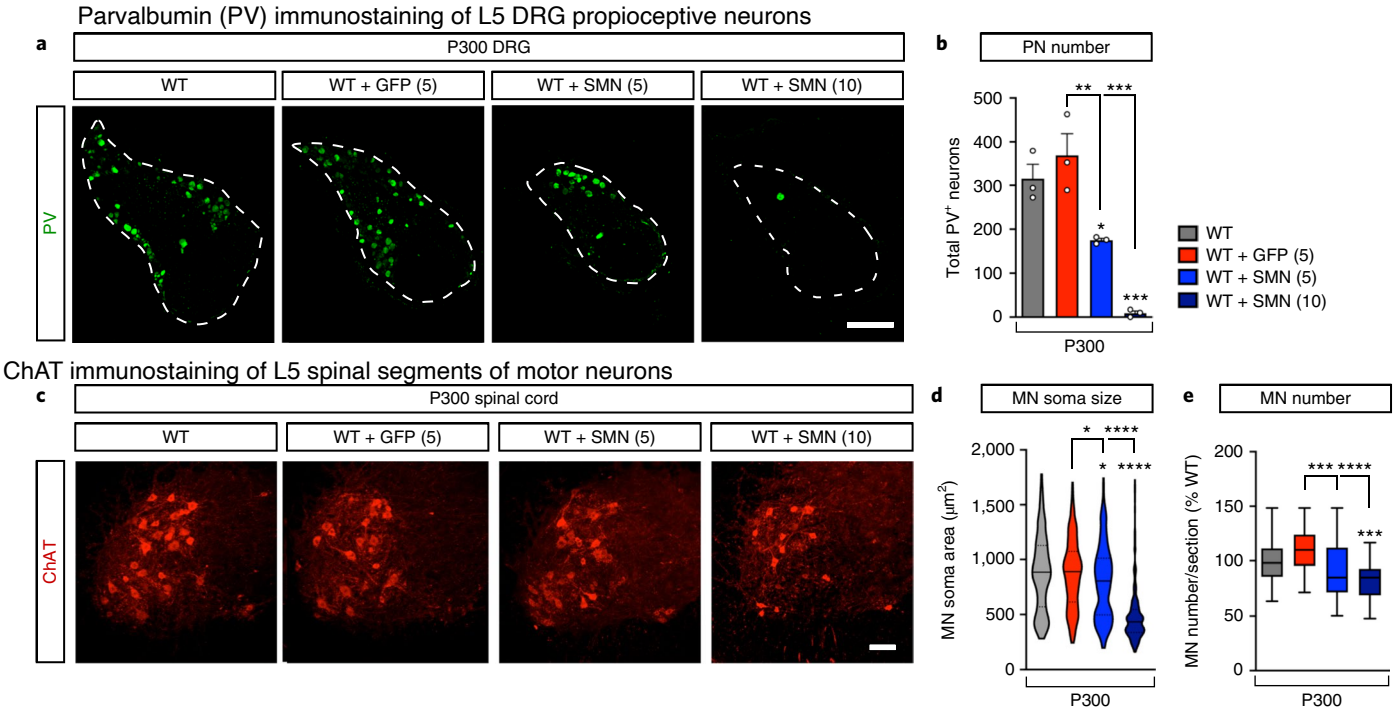


**Fig. 3 | AAV9-SMN induces late-onset neurodegeneration in WT mice. a**, Parvalbumin (PV) immunostaining of L5 DRG from uninjected, AAV9-GFP (5) and AAV9-SMN (5 and 10)-injected WT mice at P300. Scale bar, 250 µm. **b**, Total number of proprioceptive neurons (PNs) in L5 DRG from the same groups as in **a**. Data represent the mean and s.e.m. ($n=3$ DRG from $n=3$ animals). Statistics were performed with one-way ANOVA with Tukey's post hoc test. $^{*}P<0.05$; $^{**}P<0.01$; $^{***}P<0.001$. WT versus SMN (5): $P=0.0463$, $q=4.606$, d.f. = 8; WT versus SMN (10): $P=0.0005$, $q=10.07$, d.f. = 8; GFP versus SMN (5): $P=0.0087$, $q=6.350$, d.f. = 8; GFP versus SMN (10): $P=0.0001$, $q=11.81$, d.f. = 8. **c**, ChAT immunostaining of L5 spinal segments from uninjected, AAV9-GFP (5) and AAV9-SMN (5 and 10)-injected WT mice at P300. Scale bar, 100 µm. **d**, Soma size of motor neurons (MNs) from the same groups as in **c** at P300. The violin plot shows the median (solid line) and interquartile range (dotted lines) from the following number of MNs from three animals per group: WT, $n=253$ neurons; WT + GFP (5), $n=271$ neurons; WT + SMN (5), $n=251$ neurons; WT + SMN (10), $n=258$ neurons. Statistics were performed with one-way ANOVA with Tukey's post hoc test. $^{*}P<0.05$; $^{****}P<0.0001$. WT versus SMN (5): $P=0.0138$, $q=4.272$, d.f. = 1026; WT versus SMN (10): $P<0.0001$, $q=19.98$, d.f. = 1,026; GFP versus SMN (5): $P=0.0248$, $q=3.995$, d.f. = 1,026; GFP versus SMN (10): $P<0.0001$, $q=19.99$, d.f. = 1,026. **e**, Percentage of the number of L5 LMC MNs per 75-µm section relative to WT in the same groups as in **c** at P300. The box-and-whiskers graph shows the median, interquartile range and minimum and maximum from the following number of sections and animals per group (WT, $n=48$ sections, $n=3$ animals; WT + GFP (5), $n=48$ sections, $n=3$ animals; WT + SMN (5), $n=46$ sections, $n=3$ animals; WT + SMN (10), $n=55$ sections, $n=4$ animals). Statistics were performed with one-way ANOVA with Tukey's post hoc test. $^{***}P<0.001$; $^{****}P<0.0001$. WT versus SMN (10): $P=0.0001$, $q=6.218$, d.f. = 193; GFP versus SMN (5): $P=0.0005$, $q=5.680$, d.f. = 193; GFP versus SMN (10): $P<0.0001$, $q=9.531$, d.f. = 193.

Fig. 6a,c). SMN aggregates are widespread and present in over 85% of motor neurons and ~90% of proprioceptive neurons in AAV9-SMN-treated WT mice at P300 (Extended Data Fig. 6b,d), consistent with the transduction efficiency of these neurons by AAV9 (Extended Data Fig. 4a,b). Large cytoplasmic aggregates of SMN are also present in ~70% of motor neurons and ~80% of proprioceptive neurons from SMA mice injected with AAV9-SMN at P190 (Extended Data Fig. 6e–h).

Collectively, these experiments show that AAV9-mediated gene delivery leads to massive levels of prolonged transgene overexpression in neural tissue that instead decreases over time in regenerative tissue such as the liver. This reflects the high viral load, strong tropism of AAV9 for sensorimotor circuit neurons and their postmitotic nature that prevents dilution of the episomally maintained AAV9 genome—collectively making these neurons at increased risk for toxicities associated with long-term SMN overexpression. Importantly, the accumulation into large cytoplasmic aggregates in highly transduced neurons of the sensorimotor circuit reveals an abnormal feature of AAV9-mediated SMN overexpression.

**SMN overexpression impairs spliceosomal snRNP biogenesis.** The SMN protein self-oligomerizes and associates with Gemin proteins to form the core SMN complex that functions in the assembly of small nuclear ribonucleoprotein particles (snRNPs)[30]. In the absence of corresponding amounts of Gemins, it is conceivable that overexpressed SMN might engage its direct protein targets but yield nonfunctional complexes that remain stalled in the cytoplasm, thereby acting in a dominant negative manner. To determine whether SMN aggregates could indeed exert toxic effects by trapping physiological substrates, we monitored SmB—a member of the Sm core that is assembled on small nuclear RNAs by SMN in the cytoplasm before their nuclear import as snRNPs[30]. While displaying the expected nuclear localization in neurons from control mice, SmB accumulated in cytoplasmic aggregates in motor neurons and proprioceptive neurons of AAV9-SMN-injected WT and SMA mice that showed time-dependent increases in size similar to those of SMN (Fig. 5c,d and Extended Data Fig. 7). Moreover, double immunostaining of SMN and SmB in motor neurons and proprioceptive neurons of WT mice injected with AAV9-SMN demonstrated their colocalization in the same cytoplasmic aggregates (Fig. 5e,f). Importantly, nuclear snRNP levels measured by SmB fluorescence intensity were reduced in both neuronal types from AAV9-SMN-injected WT mice relative to controls at P300 (Fig. 5g,h), an SMA-like feature consistent with impaired cytoplasmic assembly of Sm cores[2,31,32].

To determine the selectivity of SmB sequestration, we analyzed several other RNA-binding proteins but found no accumulation in SMN aggregates of motor neurons transduced by AAV9-SMN (Extended Data Fig. 8a–h). We also found that SMN aggregates were neither co-labeled by ubiquitin nor by the autophagy marker LC3B (Extended Data Fig. 8i,j), indicating they are not engaged with protein degradation machinery. Lastly, to rule out that cytoplasmic aggregation of SMN and sequestration of SmB protein is related to species-specific differences of expressing human SMN in the mouse background, we overexpressed either GFP or SMN in HeLa cells by lentiviral transduction. Akin to sensorimotor circuit neurons in vivo, overexpressed SMN but not GFP induced large aggregates that sequestered endogenous SmB in cultured human cells (Extended Data Fig. 9). Thus, notwithstanding additional modes of toxicity, long-term overexpression of SMN induces cytoplasmic aggregates that specifically sequester Sm proteins, leading to impairment of snRNP biogenesis and consequent reduction in the nuclear pool of snRNPs through toxic gain of function.

**Long-term SMN overexpression induces widespread transcriptome abnormalities in DRG neurons.** The global effects of AAV9-SMN on gene expression and pre-mRNA splicing have not been investigated before. To follow up on potential downstream events of dysregulated snRNP biogenesis, we performed RNA-sequencing (RNA-seq) analysis of lumbar DRG neurons from WT mice at P300 that were untreated or injected with either AAV9-GFP or AAV9-SMN. We identified 405 high-confidence splicing changes specifically induced by AAV9-SMN relative to both AAV9-GFP-injected and uninjected WT mice (Fig. 6a and Supplementary Table 1). Differentially spliced individual cassette exons (51%) and intron retention (18%) were the most common SMN-dependent changes (Fig. 6b). Moreover, decreased inclusion of alternatively spliced exons and increased retention of introns accounted for the vast majority of these changes (Fig. 6c and Supplementary Table 1), consistent with expected effects of reduced snRNP availability on splicing[33].

We also found widespread transcriptome alterations associated with AAV9-SMN gene delivery, while AAV9-GFP had essentially no effects at the mRNA level (Fig. 6d–f). We identified 531 differentially expressed mRNAs in DRG neurons of AAV9-SMN-injected mice relative to both AAV9-GFP-injected and uninjected WT mice (Fig. 6g and Supplementary Table 2). Interestingly, Gene Ontology (GO) analysis identified strong induction of genes associated with neuroinflammation and the innate immune response (Fig. 6h). Collectively, these changes likely reflect system-level events downstream of SMN-dependent neuronal insults. Of note, these include upregulation of all three subunits of the C1q complex (Fig. 6i–k), which mediates diverse immune surveillance activities in development and disease of the CNS including synaptic pruning[34] and has been directly implicated in the loss of proprioceptive synapses in mouse models of SMA[35]. It is also conceivable that alterations in the expression of cell surface and adhesion molecules that are of crucial importance for neuronal survival and function as well as regulation of immune responses contribute to the observed neurodegenerative processes induced by AAV9-SMN (Fig. 6h)[36]. One relevant example is the observed downregulation of chondrolectin (Chodl) mRNA (Fig. 6l), the dysregulation of which has previously been implicated in SMA neuropathology[37]. Thus, while causality between specific gene changes identified above and neurotoxicity remains to be established, long-term AAV9-mediated SMN overexpression induces splicing dysregulation and widespread transcriptome alterations that can have pathogenic effects in neural tissue.

## Discussion

Our study provides direct evidence of late-onset toxicity specifically induced by AAV9-mediated SMN overexpression in the sensorimotor circuit, adding a new aspect that needs careful consideration for the long-term safety of SMA gene therapy. Together with a previous study[20] and recent safety findings that led to halting of intrathecal gene delivery in individuals with SMA[21], features of sensory neurotoxicity of AAV9-SMN have emerged across different delivery modes (intravenous and intrathecal), genetic drivers (GUSB and CBA) and animal models (mice, piglets and nonhuman primates). Importantly, mechanisms of toxicity were unknown and never previously associated with SMN-intrinsic deleterious effects as it was widely assumed that excess SMN would not be harmful. However, the potential for gain of toxic function by overexpression of SMN has been overlooked. Accordingly, we reveal slow-progressing, neuron-specific toxicity elicited by high levels of SMN that accumulate in transduced, nondividing neurons and sequester endogenous snRNP proteins—a scenario that bears analogies with neurodegenerative diseases driven by accumulation of RNA–protein aggregates[38]. The progressive erosion of snRNP biogenesis is a plausible mechanism by which SMN aggregates could contribute to RNA dysregulation and neuronal death and dysfunction in the long term (Extended Data Fig. 10). Thus, our findings in mouse models reveal that AAV9-SMN gene therapy can have opposing effects by inducing late-onset neurotoxicity in the same neurons in which it provides early functional correction of SMA deficits. They also highlight an unanticipated scenario where both a strong excess and deficiency in SMN have detrimental effects on sensorimotor circuitry.

We highlight dose dependency in the time of onset and severity of behavioral deficits and neurodegenerative processes induced by AAV9-SMN in mouse models. Differences in the level of SMN overexpression likely account for the delayed onset and milder toxicity we observed in SMA mice compared to WT mice. Similarly, previous studies in mouse models harboring multiple copies of human SMN transgenes did not reveal overt sensorimotor deficits because the level of SMN overexpression specifically in motor circuit neurons was likely much lower than that achieved with AAV9-SMN when the wider expression profile of transgenes is weighed against the restricted tropism of AAV9 in spinal cord[39,40]. While largely underestimated by protein analysis of whole-tissue lysates, the level of SMN overexpression generated by AAV9-mediated gene delivery

**Fig. 4 | AAV9 drives long-term transgene overexpression in motor neurons and proprioceptive neurons but not the liver of WT mice. a**, DAPI, GFP and either ChAT or PV immunostaining of L5 spinal cords and DRGs, as well as livers from uninjected and AAV9-GFP (5)-injected WT mice at P11 and P300. Scale bar, 250 µm. **b**, Western blot analysis of spinal cord from uninjected and either AAV9-GFP (5) or AAV9-SMN (5)-injected WT mice at P11 and P300. SMN expression was analyzed with antibodies that specifically detect only human SMN (hSMN) or both human and mouse SMN (pan-SMN). Cropped images are shown. **c**, Quantification of SMN protein levels from the western blot analysis in **b**. Data represent the mean and s.e.m. ($n=3$ animals) normalized to Gapdh and expressed relative to levels in WT mice at P11 (set as 1). Statistics were performed with one-way ANOVA with Tukey's post hoc test. ***$P<0.001$; NS, no significance. WT P11 versus SMN (5) P11: $P=0.0008$, $q=8.378$, d.f. = 12; WT P11 versus SMN (5) P300: $P=0.0002$, $q=9.952$, d.f. = 12; SMN (5) P11 versus SMN (5) P300: $P=0.8671$, $q=1.574$, d.f. = 12. **d**, Western blot analysis of liver from the same groups as in **b**. SMN expression was analyzed with antibodies that specifically detect only hSMN or pan-SMN. Cropped images are shown. **e**, Quantification of SMN protein levels from the western blot analysis in **d**. Data represent the mean and s.e.m. ($n=3$ animals), normalized to Gapdh and expressed relative to levels in WT mice at P11 (set as 1). Statistics were performed with one-way ANOVA with Tukey's post hoc test. ****$P<0.0001$. WT P11 versus SMN (5) P11: $P<0.0001$, $q=11.93$, d.f. = 12; SMN (5) P11 versus SMN (5) P300: $P<0.0001$, $q=10.95$, d.f. = 12.

is massive in motor neurons and proprioceptive neurons of mouse models, and the cytoplasmic sequestration of Sm proteins occurs similarly across normal and disease genetic backgrounds. Together with the striking analogies in downstream phenotypic effects, the most conservative interpretation is that toxic mechanisms elicited by SMN overexpression in the sensorimotor circuit are shared in WT and SMA mice. Additionally, the inclusion of WT mice in our study was critical to establish proof of concept for neuronal toxicity of overexpressed SMN in vivo and to draw conclusions without the potentially confounding elements of SMA pathology that affect the same neurons of the spinal sensorimotor circuit and RNA pathways in mouse models of the disease.

Our findings reveal an unanticipated mechanism of toxicity specifically associated with long-term AAV9-mediated overexpression

AAV9 drives long-term transgene overexpression in motor neurons and proprioceptive neurons but not the liver of WT mice

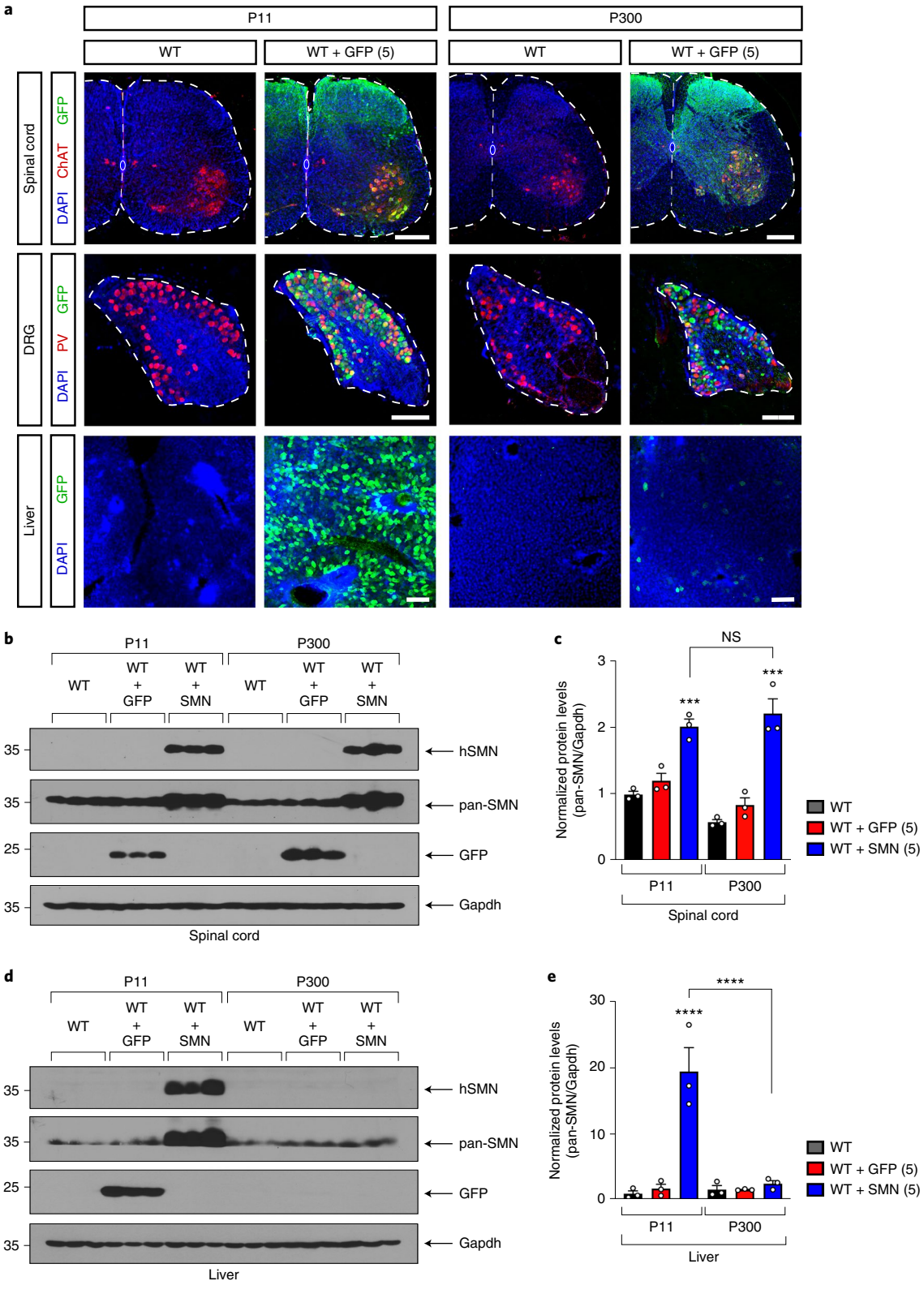

nuclear gems

SmB—a member of the Sm core that is assembled on small nuclear RNAs by SMN in the cytoplasm before their nuclear import as snRNPs

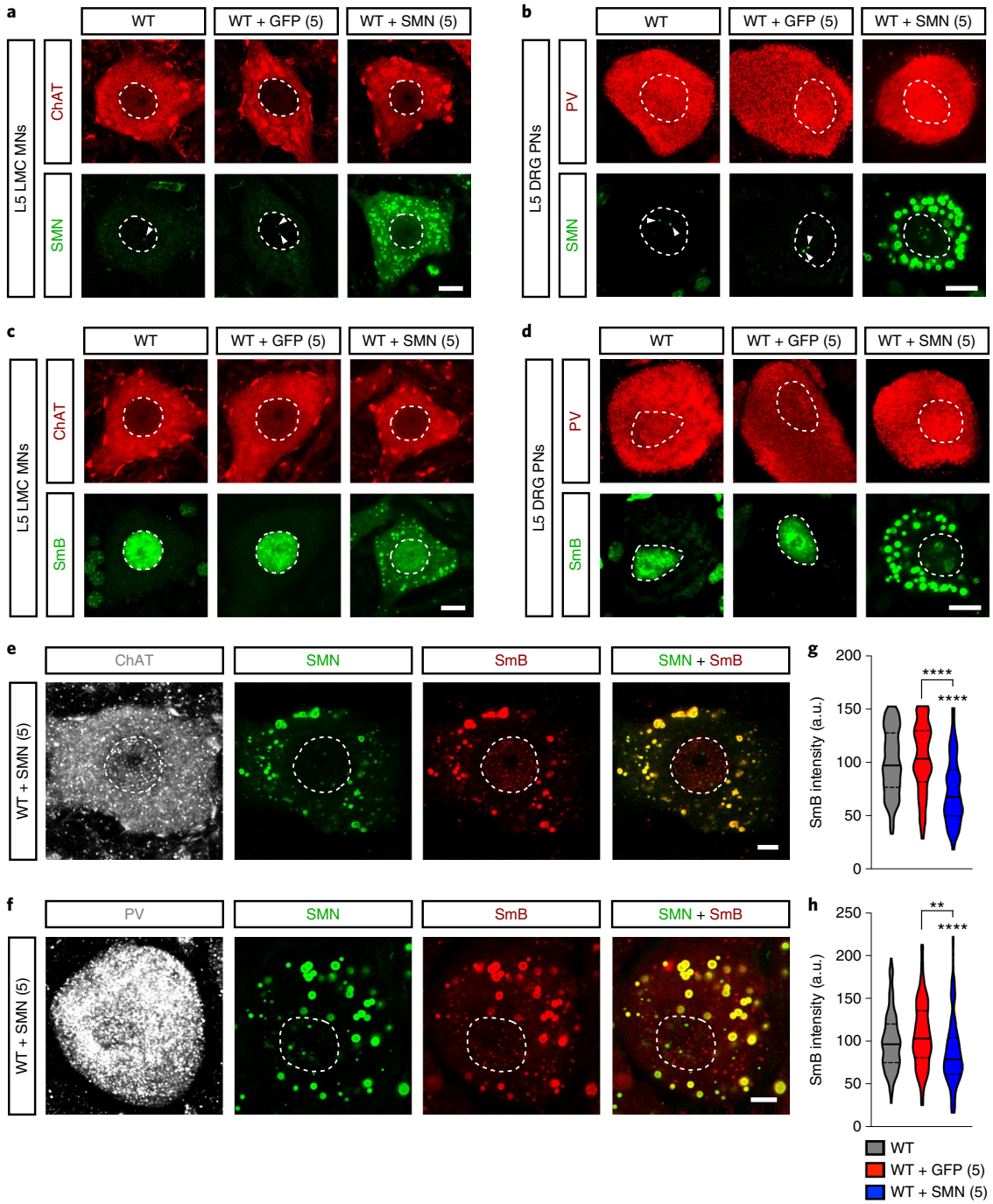


**Fig. 5 | AAV9-SMN induces cytoplasmic aggregation of SMN and SmB proteins. a**, ChAT and SMN immunostaining of L5 LMC MNs from WT mice uninjected and injected with AAV9-GFP (5) or AAV9-SMN (5) at P300. Scale bar, 10 µm. Arrowheads point to nuclear gems. **b**, PV and SMN immunostaining of L5 DRG PNs from the same groups as in **a** at P300. Scale bar, 10 µm. Arrowheads point to nuclear gems. **c**, ChAT and SmB immunostaining of L5 LMC MNs from the same groups as in **a** at P300. Scale bar, 10 µm. **d**, PV and SmB immunostaining of L5 DRG PNs from the same groups as in **a** at P300. Scale bar, 10 µm. **e**,**f**, PV, ChAT, SMN and SmB immunostaining of L5 LMC MNs (**e**) and PNs (**f**) in WT mice injected with AAV9-SMN (5) at P300. Scale bar, 5 µm. **g**,**h**, Normalized nuclear SmB fluorescence intensity in L5 LMC MNs (**g**) and PNs (**h**) from the same groups as in **e** and **f** at P300. The violin plots show the median (solid line) and interquartile range (dotted lines) from the following number of MNs (WT, $n=210$ neurons; WT + GFP (5), $n=266$ neurons; WT + SMN (5), $n=234$ neurons) and PNs (WT, $n=172$ neurons; WT + GFP (5), $n=186$ neurons; WT + SMN (5), $n=174$ neurons) from three mice per group. a.u., arbitrary units. Statistics were performed with one-way ANOVA with Tukey's post hoc test. $^{**}P<0.01$; $^{****}P<0.0001$. For MNs, WT versus SMN (5): $P<0.0001$, $q=12.99$, d.f. = 707; GFP (5) versus SMN (5): $P<0.0001$, $q=15.37$, d.f. = 707. For PNs, WT versus SMN (5): $P=0.0036$, $q=4.589$, d.f. = 529; GFP (5) versus SMN (5): $P<0.0001$, $q=7.422$, d.f. = 529.

of SMN in the sensorimotor circuit and involves—but is not necessarily limited to—inhibition of SMN's normal function in RNA regulation, which induces SMA-like functional abnormalities including loss of proprioceptive synapses and neurodegeneration. The initial trigger is accumulation of SMN in excess over endogenous levels of core subunits of the SMN complex that are required for

The splicing events include cassette exons (CAS), intron retention (IRET), alternative 3′ splice sites (ALT 3′), alternative 5′ splice sites (ALT 5′), tandem cassette exons (TACA) and mutually exclusive exons (MUTX)

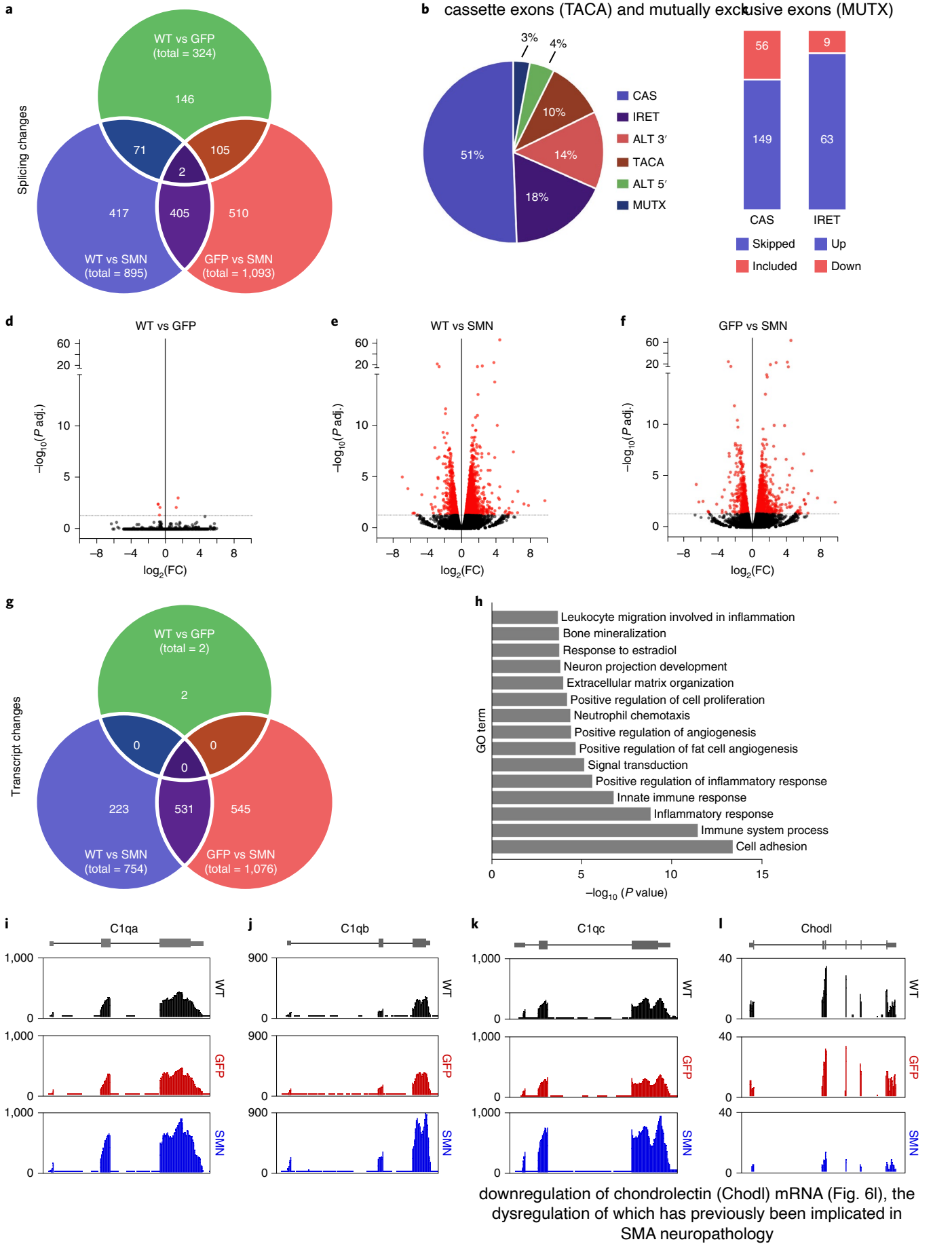


downregulation of chondrolectin (Chodl) mRNA (Fig. 6l), the dysregulation of which has previously been implicated in SMA neuropathology

**Fig. 6 | Long-term AAV9-mediated SMN overexpression induces widespread transcriptome alterations in DRGs. a**, Venn diagram of the number of splicing changes in lumbar DRGs from uninjected mice and WT mice treated with either AAV9-GFP (5) or AAV9-SMN (5) at P300 (change of percent spliced-in value ($|\Delta PSI|$) ≥ 0.1; false discovery rate (FDR) ≤ 0.05). **b**, Pie chart of the proportion of different types of splicing changes induced by AAV9-SMN in DRG neurons of WT mice. The splicing events include cassette exons (CAS), intron retention (IRET), alternative 3′ splice sites (ALT 3′), alternative 5′ splice sites (ALT 5′), tandem cassette exons (TACA) and mutually exclusive exons (MUTX). **c**, Bar graph of the number of skipped and included cassette exons, as well as increased and decreased intron retention events induced by AAV9-SMN in DRG neurons of WT mice at P300. **d**–**f**, Volcano plots of the indicated two-way comparisons of transcript-level changes in lumbar DRG neurons from uninjected mice and WT mice treated with either AAV9-GFP (5) or AAV9-SMN (5) at P300. FC, fold change. Significant changes with a multiple-testing adjusted *P* value (*P* adj.) < 0.05 using edgeR are shown in red. **g**, Venn diagram of transcript-level changes in lumbar DRGs from uninjected mice and WT mice treated with either AAV9-GFP (5) or AAV9-SMN (5) at P300 (FC > 2; FDR < 0.05). **h**, GO analysis of the most enriched biological pathways associated with AAV9-SMN-dependent gene changes in lumbar DRG cells. **i**–**l**, Representative RNA-seq tracks for C1qa (**i**), C1qb (**j**), C1qc (**k**) and Chodl (**l**) reads from lumbar DRG neurons of uninjected mice and WT mice treated with either AAV9-GFP (5) or AAV9-SMN (5) at P300.

its function in snRNP assembly[30]. Owing to the intrinsic properties of SMN to self-oligomerize and directly bind Sm proteins[41–43], it is conceivable that SMN overload promotes the formation of nonfunctional complexes that sequester Sm proteins in cytoplasmic aggregates with consequent progressive impairment of snRNP biogenesis and function. Accordingly, we show that AAV9-SMN leads to reduced snRNP levels in the nuclei of sensorimotor circuit neurons and splicing dysregulation consistent with defective snRNP abundance. Thus, our results mechanistically link overexpression of SMN to downstream functional perturbations of the splicing machinery. They also document widespread transcriptome changes induced by AAV9-SMN that highlight unintended, potentially damaging molecular signatures of this gene therapy in neural tissue.

Studies in animal models can reliably identify potentially relevant clinical liabilities of SMA gene therapy. Previous work in mice revealed dose-dependent cardiac and hepatic toxicities following intravenous administration of AAV9-SMN, and target organ toxicity was associated with mortality at doses twofold above the recommended clinical dose[44]. Acute liver toxicity was also found in nonhuman primates following intravenous administration of an AAV9-like SMN vector[20]. Although apparently not as life-threatening as in animal models, transient liver toxicity is observed in individuals with SMA treated by intravenous AAV9-SMN gene therapy[16,17,22,44]. However, unlike these early-onset adverse events likely associated with systemic exposure to high doses of AAV9 in peripheral organs[16,20,45], the neurotoxic effects leading to late-onset synaptic loss and neuronal death, as well as progressive sensorimotor dysfunction documented here, are specifically dependent on SMN overexpression. It is possible that the same mechanisms are responsible for DRG pathology induced by AAV9-SMN in piglets and nonhuman primates[20,22], on the basis of which intrathecal delivery in individuals with SMA was recently put on clinical hold[21]. In consideration of the very young age, extreme clinical severity and relatively limited time since treatment[16,17], it is plausible that individuals with type 1 SMA who received treatment with AAV9-SMN do not yet present clinical signs of neurotoxicity or that they cannot be evaluated effectively for sensory deficits due to the coarse nature of functional tests for their age. Further, neurotoxicity might appear at a later time and be especially relevant in individuals with milder SMA that have higher *SMN2* copy numbers and less compromised motor function or those who will receive intrathecal administration of AAV9-SMN. Indeed, delivery mode may serve as a key modulator of toxicity, as the degree of transduction of sensory neurons can differ following systemic or intrathecal administration of AAV9 (ref. [46]). Importantly, one of two individuals with SMA deceased to date who received treatment systemically with Zolgensma showed DRG abnormalities including ganglion cell loss and the presence of inflammatory cells[22]. This indicates that DRG neuropathology is not restricted to animal models and may extend to AAV9-SMN-treated individuals with SMA. As postmortem tissue becomes available in the future, it would be important to determine whether cytoplasmic aggregation of SMN and sequestration of Sm proteins occurs in DRG neurons and spinal motor neurons of Zolgensma-treated individuals with SMA. Moreover, monitoring changes in the amplitude of H-reflexes over time in a clinical setting could be helpful to identify any evidence of sensory neurotoxicity in individuals treated by gene therapy.

The induction of inflammatory and immune responses in DRGs appears to be a conserved feature of AAV9-SMN treatment in animal models, the origins and consequences of which are incompletely understood. It has been proposed that systemic delivery of high doses of AAV drives DRG neuropathology in piglet and nonhuman primates injected with an AAV9-like SMN vector independent of an immune response against the capsid or the transgene[20], but the study was not designed to directly distinguish between these possibilities. Our findings that sensorimotor circuit pathology is specifically associated with AAV9-SMN but not AAV9-GFP argue against a prominent contribution of immune responses directed against the AAV9 capsid as well as other transgene-independent mechanisms to neurotoxicity in vivo. Moreover, while human and mouse SMN proteins are 82% identical and an even higher identity (>90%) is shared between human and either porcine or nonhuman primate SMN[47,48], an adaptive immune response to human SMN could be another contributing factor to the toxicity of AAV9-SMN in naïve animal models. However, although we have not tested this experimentally in mice, a robust T-cell response against overexpressed human SMN was not found in piglets and nonhuman primates[20]. Additionally, we show that AAV9-SMN is neurotoxic in SMNΔ7 SMA mice in which human SMN is not a foreign antigen. Therefore, we argue that the observed signatures of inflammation and immune response in DRG cells are secondary events downstream of initial intrinsic insults triggered by overexpression of SMN in neurons. Moving forward, mechanistic studies are required to determine the precise nature of the inflammatory and immune responses, as well as their potential contribution to neurotoxicity induced by AAV9-SMN.

In conclusion, the gain of toxic function of SMN overexpression is a newly identified aspect of SMN biology that has clinically relevant implications due to the current use of AAV9-SMN for the treatment of individuals with SMA. It provides a conceptual framework to explain the unanticipated adverse effects of AAV9-SMN in the sensorimotor circuit of animal models and provides a note of caution regarding the use of SMA gene therapy in humans. Together with the plausible irreversibility of sustained SMN overload in neurons driven by AAV9-SMN gene therapy, this knowledge will impact the cost–benefit evaluation of gene therapy relative to other available options and be helpful for guiding individuals to make informed decisions about which SMA treatment to pursue. Our findings suggest that late-onset neurodegenerative pathology might follow early clinical benefits in individuals treated with AAV9-SMN. They also provide a compelling case for potential risks associated

with uncontrolled, long-lasting transgene expression especially in neurons. This has broader therapeutic implications beyond SMA and underscores the general importance of embedding tunable on/off switches in gene therapy vectors as de-risking strategies against unwanted protein toxicities.

## Online content

Any methods, additional references, Nature Research reporting summaries, source data, extended data, supplementary information, acknowledgements, peer review information; details of author contributions and competing interests; and statements of data and code availability are available at https://doi.org/10.1038/s41593-021-00827-3.

Received: 4 September 2020; Accepted: 24 February 2021;
Published online: 1 April 2021

## References

1. Burghes, A. H. M. & Beattie, C. E. Spinal muscular atrophy: why do low levels of survival motor neuron protein make motor neurons sick? *Nat. Rev. Neurosci.* **10**, 597–609 (2009).
2. Tisdale, S. & Pellizzoni, L. Disease mechanisms and therapeutic approaches in spinal muscular atrophy. *J. Neurosci.* **35**, 8691–8700 (2015).
3. Lefebvre, S. et al. Identification and characterization of a spinal muscular atrophy-determining gene. *Cell* **80**, 155–165 (1995).
4. Lorson, C. L., Hahnen, E., Androphy, E. J. & Wirth, B. A single nucleotide in the *SMN* gene regulates splicing and is responsible for spinal muscular atrophy. *Proc. Natl Acad. Sci. USA* **96**, 6307–6311 (1999).
5. Hua, Y. et al. Peripheral SMN restoration is essential for long-term rescue of a severe spinal muscular atrophy mouse model. *Nature* **478**, 123–126 (2011).
6. Porensky, P. N. et al. A single administration of morpholino antisense oligomer rescues spinal muscular atrophy in mouse. *Hum. Mol. Genet.* **21**, 1625–1638 (2012).
7. Naryshkin, N. A. et al. Motor neuron disease. SMN2 splicing modifiers improve motor function and longevity in mice with spinal muscular atrophy. *Science* **345**, 688–693 (2014).
8. Palacino, J. et al. SMN2 splice modulators enhance U1-pre-mRNA association and rescue SMA mice. *Nat. Chem. Biol.* **11**, 511–517 (2015).
9. Foust, K. D. et al. Rescue of the spinal muscular atrophy phenotype in a mouse model by early postnatal delivery of SMN. *Nat. Biotechnol.* **28**, 271–274 (2010).
10. Passini, M. A. et al. CNS-targeted gene therapy improves survival and motor function in a mouse model of spinal muscular atrophy. *J. Clin. Invest.* **120**, 1253–1264 (2010).
11. Dominguez, E. et al. Intravenous scAAV9 delivery of a codon-optimized SMN1 sequence rescues SMA mice. *Hum. Mol. Genet.* **20**, 681–693 (2011).
12. Valori, C. F. et al. Systemic delivery of scAAV9 expressing SMN prolongs survival in a model of spinal muscular atrophy. *Sci. Transl. Med.* **2**, 35ra42 (2010).
13. Finkel, R. S. et al. Nusinersen versus sham control in infantile-onset spinal muscular atrophy. *N. Engl. J. Med.* **377**, 1723–1732 (2017).
14. Finkel, R. S. et al. Treatment of infantile-onset spinal muscular atrophy with nusinersen: a phase 2, open-label, dose-escalation study. *Lancet* **388**, 3017–3026 (2016).
15. Mercuri, E. et al. Nusinersen versus sham control in later-onset spinal muscular atrophy. *N. Engl. J. Med.* **378**, 625–635 (2018).
16. Mendell, J. R. et al. Single-dose gene-replacement therapy for spinal muscular atrophy. *N. Engl. J. Med.* **377**, 1713–1722 (2017).
17. Al-Zaidy, S. et al. Health outcomes in spinal muscular atrophy type 1 following AVXS-101 gene replacement therapy. *Pediatr. Pulmonol.* **54**, 179–185 (2019).
18. Dhillon, S. Risdiplam: first approval. *Drugs* **80**, 1853–1858 (2020).
19. Mercuri, E., Pera, M. C., Scoto, M., Finkel, R. & Muntoni, F. Spinal muscular atrophy—insights and challenges in the treatment era. *Nat. Rev. Neurol.* https://doi.org/10.1038/s41582-020-00413-4 (2020).
20. Hinderer, C. et al. Severe toxicity in nonhuman primates and piglets following high-dose intravenous administration of an adeno-associated virus vector expressing human SMN. *Hum. Gene Ther.* **29**, 285–298 (2018).
21. National Library of Medicine. Study of intrathecal administration of onasemnogene abeparvovec-xioi for spinal muscular atrophy (STRONG). *ClinicalTrials.gov* https://clinicaltrials.gov/ct2/show/NCT03381729 (2017).
22. European Medicines Agency. Zolgensma: European public assessment report. https://www.ema.europa.eu/en/documents/assessment-report/zolgensma-epar-public-assessment-report_en.pdf (2020).
23. Passini, M. A. et al. Translational fidelity of intrathecal delivery of self-complementary AAV9-survival motor neuron 1 for spinal muscular atrophy. *Hum. Gene Ther.* **25**, 619–630 (2014).
24. Gray, S. J. & Samulski, R. Vector design and considerations for CNS applications. in *Gene Vector Design and Application to Treat Nervous System Disorders* (ed. Glorioso. J.) 7–15 (Society for Neuroscience, 2011).
25. Taylor, M. D. et al. Postnatal regulation of limb proprioception by muscle-derived neurotrophin-3. *J. Comp. Neurol.* **432**, 244–258 (2001).
26. Simon, C. M. et al. Stasimon contributes to the loss of sensory synapses and motor neuron death in a mouse model of spinal muscular atrophy. *Cell Rep.* **29**, 3885–3901 (2019).
27. Mentis, G. Z. et al. Early functional impairment of sensorimotor connectivity in a mouse model of spinal muscular atrophy. *Neuron* **69**, 453–467 (2011).
28. Fletcher, E. V. et al. Reduced sensory synaptic excitation impairs motor neuron function via Kv2.1 in spinal muscular atrophy. *Nat. Neurosci.* **20**, 905–916 (2017).
29. Simon, C. M. et al. Converging mechanisms of p53 activation drive motor neuron degeneration in spinal muscular atrophy. *Cell Rep.* **21**, 3767–3780 (2017).
30. Li, D. K., Tisdale, S., Lotti, F. & Pellizzoni, L. SMN control of RNP assembly: from post-transcriptional gene regulation to motor neuron disease. *Semin. Cell Dev. Biol.* **32**, 22–29 (2014).
31. Ruggiu, M. et al. A role for SMN exon 7 splicing in the selective vulnerability of motor neurons in spinal muscular atrophy. *Mol. Cell. Biol.* **32**, 126–138 (2012).
32. Van Alstyne, M. et al. Dysregulation of Mdm2 and Mdm4 alternative splicing underlies motor neuron death in spinal muscular atrophy. *Genes Dev.* **32**, 1045–1059 (2018).
33. Saltzman, A. L., Pan, Q. & Blencowe, B. J. Regulation of alternative splicing by the core spliceosomal machinery. *Genes Dev.* **25**, 373–384 (2011).
34. Tenner, A. J., Stevens, B. & Woodruff, T. M. New tricks for an ancient system: physiological and pathological roles of complement in the CNS. *Mol. Immunol.* **102**, 3–13 (2018).
35. Vukojicic, A. et al. The classical complement pathway mediates microglia-dependent remodeling of spinal motor circuits during development and in SMA. *Cell Rep.* **29**, 3087–3100 (2019).
36. Lucin, K. M. & Wyss-Coray, T. Immune activation in brain aging and neurodegeneration: too much or too little? *Neuron* **64**, 110–122 (2009).
37. Sleigh, J. N. et al. Chondrolectin affects cell survival and neuronal outgrowth in in vitro and in vivo models of spinal muscular atrophy. *Hum. Mol. Genet.* **23**, 855–869 (2014).
38. Nussbacher, J. K., Tabet, R., Yeo, G. W. & Lagier-Tourenne, C. Disruption of RNA metabolism in neurological diseases and emerging therapeutic interventions. *Neuron* **102**, 294–320 (2019).
39. Monani, U. R. The human centromeric survival motor neuron gene (*SMN2*) rescues embryonic lethality in *Smn*$^{-/-}$ mice and results in a mouse with spinal muscular atrophy. *Hum. Mol. Genet.* **9**, 333–339 (2000).
40. Gavrilina, T. O. et al. Neuronal SMN expression corrects spinal muscular atrophy in severe SMA mice while muscle-specific SMN expression has no phenotypic effect. *Hum. Mol. Genet.* **17**, 1063–1075 (2008).
41. Lorson, C. L. et al. SMN oligomerization defect correlates with spinal muscular atrophy severity. *Nat. Genet.* **19**, 63–66 (1998).
42. Pellizzoni, L., Charroux, B. & Dreyfuss, G. SMN mutants of spinal muscular atrophy patients are defective in binding to snRNP proteins. *Proc. Natl Acad. Sci. USA* **96**, 11167–11172 (1999).
43. Bühler, D., Raker, V., Lührmann, R. & Fischer, U. Essential role for the tudor domain of SMN in spliceosomal U snRNP assembly: implications for spinal muscular atrophy. *Hum. Mol. Genet.* **8**, 2351–2357 (1999).
44. U.S. Food and Drug Administration. AveXis. Zolgensma (onasemnogene abeparvovec-xioi) package insert. https://www.fda.gov/vaccines-blood-biologics/zolgensma (2019).
45. Hordeaux, J. et al. The neurotropic properties of AAV-PHP.B are limited to C57BL/6J mice. *Mol. Ther.* **26**, 664–668 (2018).
46. Schuster, D. J. et al. Biodistribution of adeno-associated virus serotype 9 (AAV9) vector after intrathecal and intravenous delivery in mouse. *Front. Neuroanat.* **8**, 42 (2014).
47. DiDonato, C. J. et al. Cloning, characterization and copy number of the murine survival motor neuron gene homolog of the spinal muscular atrophy-determining gene. *Genome Res.* **7**, 339–352 (1997).
48. Lorson, M. A., Spate, L. D., Prather, R. S. & Lorson, C. L. Identification and characterization of the porcine (*Sus scrofa*) survival motor neuron (*SMN1*) gene: an animal model for therapeutic studies. *Dev. Dyn.* **237**, 2268–2278 (2008).

## Methods

**AAV9 production.** Vectors containing the open reading frames of GFP and human SMN cloned downstream of the GUSB promoter of vectors harboring AAV2 inverted terminal repeats were previously described[10]. DNA for production of AAV9 vectors was purified using endotoxin-free Mega Prep Kit (QIAGEN) according to the manufacturer's instructions. The recombinant plasmids were each packaged into AAV9 capsid by triple-plasmid transfection of human HEK293T cells, and virions were purified by CsCl gradient centrifugation as previously described[23,32]. The resulting vectors were concentrated using Amicon Ultracel centrifugal filter devices with a 30,000 nominal molecular weight limit (Millipore) and titered by qPCR. Three different vector preparations were used in this study.

**Animal procedures.** All mouse work was performed in accordance with the National Institutes of Health (NIH) Guidelines on the Care and Use of Animals, complied with all ethical regulations and was approved by the Institutional Animal Care and Use Committee of Columbia University. Mice were housed in an animal facility controlled for humidity (40–60%) and temperature (~18–23 °C) with a 12 h–12 h light–dark cycle with free access to food and water. Equal proportions of mice from both sexes were used in all experiments, and aggregated data are presented because sex-specific differences were not found. C57BL/6J mice were obtained from the Jackson Laboratory (Jax stock no. 000664). The SMNΔ7 mouse line FVB.Cg-*Grm7*$^{Tg(SMN2)89Ahmb}$ *Smn1*$^{tm1Msd}$ Tg(SMN2*delta7)4299Ahmb/J on a pure FVB/N genetic background was obtained from the Jackson Laboratory (Jax stock no. 005025) and used to generate SMA mice (*Smn*$^{-/-}$/*SMN2*$^{+/+}$/*SMNΔ7*$^{+/+}$). Genotyping of the *Smn*-knockout allele was performed using tail DNA PCR and the primers listed in Supplementary Table 3 as previously described[28]. Intracerebroventricular injections were carried out at P0 in SMNΔ7 mice and P1 in C57BL/6J mice anesthetized by isoflurane inhalation by a single injection of 5 µl in the right lateral ventricle of the brain. For AAV9 gene delivery, we delivered varying genome copies of the indicated AAV9 vectors as specified in PBS containing 5% sorbitol, 0.001% Pluronic F-68 and a vital dye (Fast Green, Sigma). Mice were euthanized and tissue collection was performed in a dissection chamber under continuous oxygenation (95% $O_2$ and 5% $CO_2$) in the presence of cold (~12 °C) artificial cerebrospinal fluid containing 128.35 mM NaCl, 4 mM KCl, 0.58 mM $NaH_2PO_4$, 21 mM $NaHCO_3$, 30 mM D-glucose, 1.5 mM $CaCl_2$ and 1 mM $MgSO_4$. Tissues were then postfixed in 4% paraformaldehyde (PFA) for immunohistochemistry or flash frozen for RNA and protein analysis.

**Mouse behavioral assays.** For the inverted-grid assay, animals were placed on a grid with 1 cm × 1 cm$^2$ squares and inverted over a 30-cm tall cylinder until falling. Three trials were performed for each animal with a cutoff time of 180 s and averaged for each data point. Animals were assayed on the inverted grid weekly, and performance over 4 weeks was averaged and reported in monthly time bins. For the rotarod assay, animals were first trained at a constant speed of 4 r.p.m. for three trials until able to perform the test. For data collection, animals were placed on the rotarod and the speed was accelerated from 4 r.p.m. to 40 r.p.m. over a period of 300 s. Three trials were performed for each animal and the times of fall were recorded and averaged for each data point. Animals were assayed on the rotarod weekly, and performance over 4 weeks was averaged and reported in monthly time bins.

**Electrophysiology.** Electromyography recordings were performed under isoflurane anesthesia (2% vaporized in $O_2$ at a flow rate of 2 l min$^{-1}$). A pair of needle electrodes was inserted in the thigh for sciatic nerve stimulation and another pair of electrodes was inserted in the hind paw for electromyogram recording of the interosseous muscles. A constant current stimulator was used to deliver short pulses (0.2 ms in duration) at different frequencies (0.1 Hz to 50 Hz). The stimulation intensity ranged from subthreshold levels for the induction of compound muscle action potentials to twice this intensity (sufficient to elicit maximal M-waves amplitude). The maximal amplitude reached throughout the stimulation intensity range for the H-reflex was acquired and stored for analysis. Body temperature was monitored and maintained at 38 °C with a heating pad during the entire recording session, and the mouse was euthanized immediately thereafter with an intraperitoneal injection of tribromoethanol (300 mg kg$^{-1}$) followed by cervical dislocation. Clampex (v10.2, Molecular Devices) software was used for data acquisition and Clampfit (v10.2, Molecular Devices) was used for data analysis.

**RNA analysis.** Purification of total RNA from mouse spinal cords and liver was carried out using TRIzol reagent (Invitrogen) per the manufacturer's instructions followed by treatment with RNase-free DNase I (Ambion). For RNA analysis from DRG neurons, total RNA was isolated using RNAqueous-Micro Kit (Ambion) including DNase I treatment. cDNA was generated using RevertAid RT Reverse Transcription Kit (Thermo Fisher Scientific) with random hexamer and oligo-dT primers. RT–qPCR analysis was performed using SYBR Green (Applied Biosystems) in technical triplicates and normalized to endogenous Gapdh mRNA levels. The primers used for RT–qPCR experiments are listed in Supplementary Table 3.

**Protein analysis.** Proteins from mouse spinal cord and liver tissue were homogenized in SDS–PAGE sample buffer and quantified using RC DC protein assay (Bio-Rad). Protein extracts were run on 12% polyacrylamide gel and transferred to nitrocellulose membranes as previously described[31]. Blocking was done in 5% milk in PBS/0.1% Tween, and primary and secondary antibodies were diluted in PBS/0.1% Tween. Chemiluminescence was carried out using a SuperSignal West Pico chemiluminescent substrate (Thermo Fisher Scientific) according to the manufacturer's instructions. Signal was detected by autoradiography using Full Speed Blue sensitive medical X-ray film (Ewen Parker X-Ray). SMN protein levels were quantified by densitometry analysis and normalized to the levels of endogenous Gapdh using Fiji (v1.0). The antibodies used for these experiments are listed in Supplementary Table 4.

**RNA sequencing and bioinformatics.** Total RNA was isolated from lumbar DRG cells using RNAqueous-Micro Kit (Ambion) followed by DNase I treatment. RNA quality and quantity were assessed using the 2100 Bioanalyzer (Agilent). Total RNA from three independent replicates per experimental group was deep sequenced with the Illumina NovaSeq 6000 platform, yielding about 80 million 2 × 100 paired-end reads per sample. RTA3 and bcl2fastq2 (v2.20) were used for base calling and conversion of sequencing data. All RNA-seq data were mapped to the reference mouse genome (mm10) and a database of exon junctions using OLego (v1.1.5)[49]. As described previously[50], the Quantas pipeline was used to perform differential splicing and gene expression analysis between WT, AAV-GFP and AAV-SMN. Briefly, to identify exons with differential splicing in two compared conditions, a two-sided Fisher's exact test with multiple-testing correction using the Benjamini–Hochberg procedure[51] to estimate FDR was used to determine the statistical significance of splicing changes using both exonic and junction reads that support each of the two splice isoforms. All the biological replicates were combined for quantification. An event was determined to be differentially spliced if the event had sufficient read coverage (coverage ≥ 20), $|\Delta PSI| \geq 0.1$ and FDR ≤ 0.05. The edgeR method included in the Quantas pipeline was used to perform differential expression analysis[52]. Statistical significance of differentially expressed genes within two compared conditions was called by requiring an FDR < 0.05 and a fold change > 2. GO analysis was performed using DAVID (v6.8)[53].

**Lentivirus transduction.** Lentiviral constructs expressing human SMN or GFP from the cytomegalovirus promoter were generated by standard cloning techniques using the pRRLSIN.cPPT.PGK-GFP.WPRE vector (Addgene plasmid no. 12252) as the initial backbone. Viral stocks pseudotyped with the vesicular stomatitis G protein were prepared by transient co-transfection of HEK293T cells (Open Biosystems) using the ViraPower Lentiviral Packaging Mix (Invitrogen) following the manufacturer's instructions. Supernatant was collected 48 h after transfection. Lentivirus was concentrated by ultracentrifugation at 19,500 r.p.m. for 2.5 h at 20 °C, reconstituted in PBS and stored in aliquots at −80 °C. The viral titer was determined with the Lenti-X qRT–PCR Titration Kit (Clontech). A multiplicity of infection of 1:1 was used to transduce HeLa cells grown in DMEM with high glucose (Invitrogen) containing 10% FBS (HyClone), 2 mM glutamine (Gibco) and 1% penicillin–streptomycin (Gibco).

**Immunofluorescence analysis.** HeLa cells were processed by immunofluorescence analysis 5 d after lentiviral transduction. Following a brief wash with PBS, cells were fixed with 4% PFA in PBS for 15 min at room temperature, and permeabilized with 0.5% Triton X-100–PBS for 10 min at room temperature. Blocking and incubation with both primary and secondary antibodies were performed at room temperature using 3% BSA in PBS for 2 h and 1 h, respectively. Images were collected with an SP5 Leica confocal microscope.

**Immunohistochemistry analysis.** For spinal cord and DRG analysis, dissected tissue was fixed in 4% PFA for 24 h, and then specific lumbar segments were identified by the ventral roots. Segments were embedded in agar and sectioned at 75 µm with a VT1000 S vibratome (Leica). Sections were blocked in 10% donkey serum in 0.01 M PBS/0.4% Triton X-100 for 1.5 h. For DRG cells stained with mouse primary antibodies, an additional blocking step with 40 µg ml$^{-1}$ of anti-mouse IgG Fab Fragment (Jackson) for 2 h in PBS was performed and then sections were incubated with primary antibodies overnight at room temperature. Six washing steps of 10 min each were done before incubation with secondary antibodies (Jackson) in PBS for 3 h at room temperature. Another six washing steps were performed before sections were mounted in 30% glycerol/PBS. For NMJ analysis of skeletal muscle (quadratus lumborum (QL) and extensor digitorum longus (EDL)), freshly dissected tissue was fixed in 4% PFA for 2 h, then cryoprotected in 30% sucrose overnight, embedded in optimal cutting temperature compound and frozen. Cryosections (30 µm) were cut and then blocked with 5% donkey serum in TBS/0.2% Triton X-100 for 1 h at room temperature before staining. Sections were incubated with primary antibodies in blocking buffer overnight at 4 °C. Following incubation, sections were washed three times for 10 min in TBS/0.2% Triton X-100, then incubated with secondary antibodies for 1 h at room temperature, followed by three washing steps. Slides were mounted with Fluoromount-G (SouthernBiotech). The antibodies used for these experiments are listed in Supplementary Table 4.

**Confocal microscopy and quantification.** All images were acquired using a Leica SP5 confocal microscope running the LAS AF software (v2.5.2.6939) and analyzed off-line using the Leica LAS X software (v1.9.0.13747) from z-stack images as previously described[27,28]. Images for the quantification of motor neuron number were acquired using a ×20 objective at 3-µm steps in the *z* axis. Images for ChAT$^+$ C-boutons and VGluT1$^+$ synapses were acquired using a ×40 objective at 0.3-µm steps in the *z* axis. The total number of ChAT$^+$ C-boutons and VGluT1$^+$ synapses on somata was determined by counting all the corresponding inputs on the surface of each motor neuron cell body. The density of VGluT1$^+$ synapses on proximal dendrites was determined by measuring the number of all VGluT1$^+$ contacts on a dendritic segment up to a distance of 50 µm from the motor neuron cell body and dividing this number by the total linear length of the dendritic segment[27]. Synaptic coverage was determined by scoring a minimum of eight motor neurons/dendrites per mouse and three or more mice for each treatment group and time point. One-way ANOVA analysis was performed to confirm that there was no statistically significant difference in the mean and variance of the number of synaptic inputs across individual mice within any treatment group. The number of synapses on somata and dendrites from all motor neurons within a group were then pooled and used for comparison with those from other treatment groups[26–29,32]. The statistical comparisons presented here are upheld when the mean of synaptic inputs is averaged per mouse (Supplementary Table 5). Images for the quantification of NMJ innervation were obtained using a ×20 objective at 2-µm steps in the *z* axis. Images for SmB intensity analysis were acquired using a ×40 objective at identical settings for WT and SMA samples at 3-µm steps, and analysis was performed using LAS X software by measuring the peak intensity per unit area of the nuclear region of motor neurons as previously described[32]. Motor neuron area was quantified as the maximum cross-sectional area of each neuron using Fiji (v1.0).

**Statistics and reproducibility.** Differences between two groups were analyzed by two-tailed unpaired Student's *t*-test, and differences among three or more groups were analyzed by one-way or two-way ANOVA followed by Tukey's post hoc tests for multiple comparisons as indicated. Comparison of survival curves was performed with the Mantel–Cox log-rank test. GraphPad Prism (v8.4.2) was used for all statistical analyses and *P* values are indicated as follows: $^*P<0.05$, $^{**}P<0.01$, $^{***}P<0.001$ and $^{****}P<0.0001$. All micrographs are representative images of at least three experiments performed with independent biological samples. No statistical methods were used to predetermine sample sizes, but our sample sizes are similar to those reported in previous publications[26–29,32]. Data distribution was assumed to be normal, but this was not formally tested. Experimental animals were randomly assigned to treatment groups. Blinding to treatment conditions was performed when running behavioral assays, sequencing experiments and electrophysiological recordings.

**Reporting Summary.** Further information on research design is available in the Life Sciences Reporting Summary linked to this article.

## Data availability

The data supporting the findings of this study are available in this paper or the Supplementary Information. Sequencing data have been deposited in the Gene Expression Omnibus database under accession number GSE149391. Source data are provided with this paper. Any other raw data that support the findings of this study are available from the corresponding author upon reasonable request.

## References


49. Wu, J., Anczuków, O., Krainer, A. R., Zhang, M. Q. & Zhang, C. OLego: fast and sensitive mapping of spliced mRNA-seq reads using small seeds. *Nucleic Acids Res.* **41**, 5149–5163 (2013).
50. Yan, Q. et al. Systematic discovery of regulated and conserved alternative exons in the mammalian brain reveals NMD modulating chromatin regulators. *Proc. Natl Acad. Sci. USA* **112**, 3445–3450 (2015).
51. Benjamini, Y. & Hochberg, Y. Controlling the false discovery rate—a practical and powerful approach to multiple testing. *J. R. Stat. Soc. Ser. B* **57**, 289–300 (1995).
52. Robinson, M. D., Mccarthy, D. J. & Smyth, G. K. edgeR: a Bioconductor package for differential expression analysis of digital gene expression data. *Bioinformatics* **26**, 139–140 (2010).
53. Huang, D. W., Sherman, B. T. & Lempicki, R. A. Systematic and integrative analysis of large gene lists using DAVID bioinformatics resources. *Nat. Protoc.* **4**, 44–57 (2009).


## Acknowledgements


We are grateful to S. Jaffrey for comments and critical reading of the manuscript. This work was supported by NIH grants R01NS102451 (to L.P.), R21NS099977 (to L.P.), R01NS078375 (to G.Z.M.) and R01AA027079 (to G.Z.M.). High-performance computation was supported by NIH grants S10OD012351 and S10OD021764. This research was funded in part through the NIH/NCI Cancer Center Support Grant P30CA013696 and used the Genomics and High-Throughput Screening Shared Resource.


## Author contributions

L.P. designed and supervised the study. M.V.A. performed the experiments and analyzed the data except as noted below. I.T. and E.W. contributed to behavioral studies. N.D. performed electrophysiological studies and data analysis. Y.R. and C.Z. carried out bioinformatic analysis of RNA-seq data. L.S.S. provided AAV9 vectors. G.Z.M. contributed to the design, analysis and interpretation of functional studies. M.V.A. and L.P. wrote the manuscript with input from all authors.

## Competing interests

The authors declare no competing interests.

## Additional information

**Extended data** is available for this paper at https://doi.org/10.1038/s41593-021-00827-3.

**Supplementary information** The online version contains supplementary material available at https://doi.org/10.1038/s41593-021-00827-3.

**Correspondence and requests for materials** should be addressed to L.P.

**Peer review information** *Nature Neuroscience* thanks the anonymous reviewers for their contribution to the peer review of this work.

**Reprints and permissions information** is available at www.nature.com/reprints.

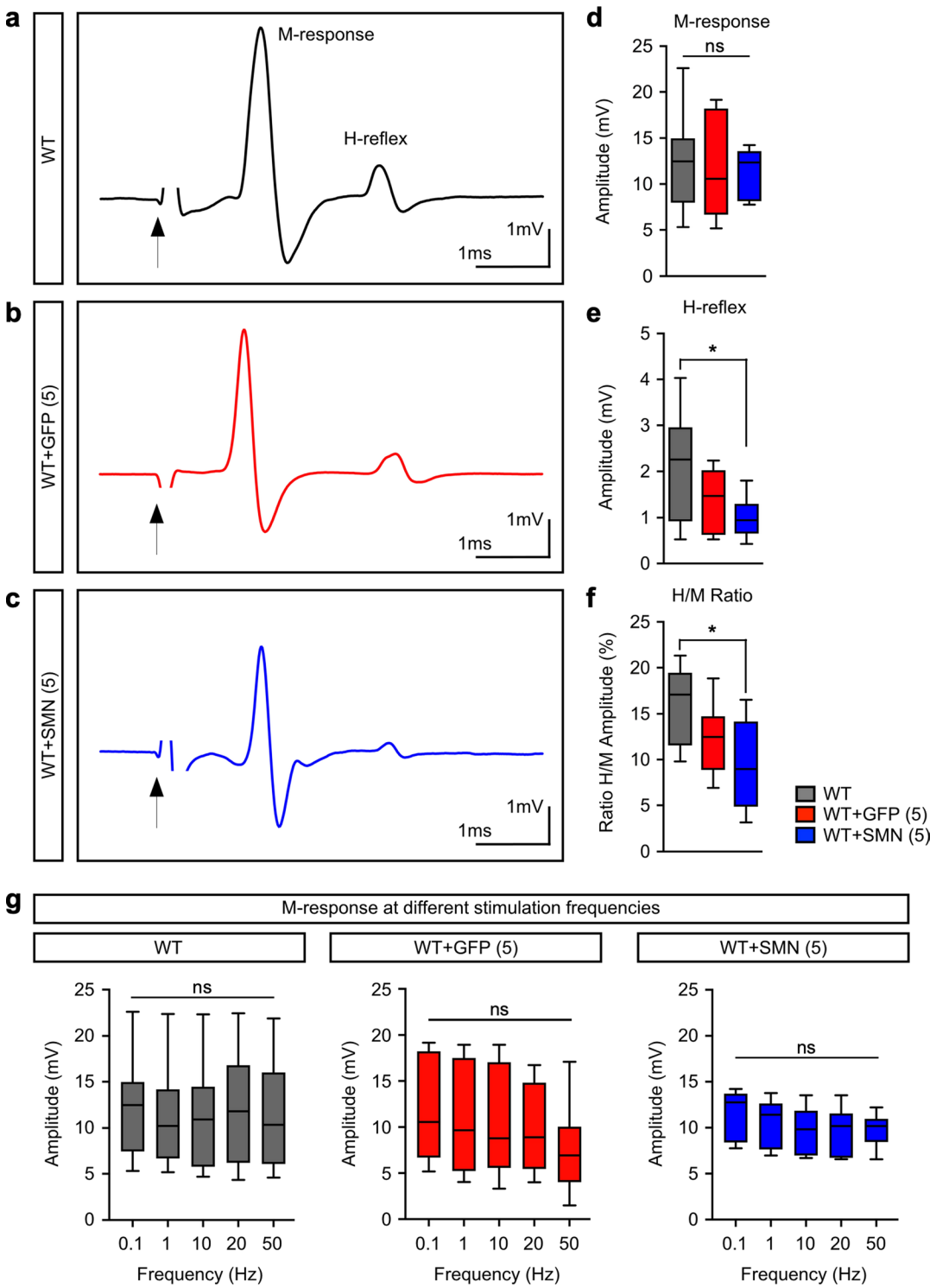


**Extended Data Fig. 1 | See next page for caption.**

**Extended Data Fig. 1 | Long-term AAV9-mediated SMN overexpression decreases sensory-motor synaptic transmission of proprioceptive neurons.** **a**-**c**, Representative EMG recordings from the footpad of uninjected (**a**) and either AAV9-GFP (5) (**b**) or AAV9-SMN (5) (**c**) treated WT mice at P300 using a stimulation frequency of 0.1 Hz. This analysis captures both proprioceptive synaptic function (H-reflex) and motor neuron function (M-response), and the H/M ratio can determine a preferential deficit in either response. Arrows point to the stimulus artifact. **d**, Amplitude of the M-response from the same groups as shown in (**a-c**). The box-and-whiskers graph shows the median, interquartile range, minimum and maximum (n = 8 animals). Statistics were performed with one-way ANOVA with Tukey's *post hoc* test. (ns) no significance. $P = 0.9741$, $F_{2, 21} = 0.02629$. **e**, Amplitude of H-reflex from the same groups as shown in (**a-c**). The box-and-whiskers graph shows the median, interquartile range, minimum and maximum (n = 8 animals). Statistics were performed with one-way ANOVA with Tukey's *post-hoc* test. (*) $P < 0.05$. WT vs SMN(5): $P = 0.0420$, $q = 3.684$, d.f.=21. **f**, Ratio of H-reflex and M-response from the same groups as shown in (**a-c**). The box-and-whiskers graph shows the median, interquartile range, minimum and maximum (n = 8 animals). Statistics were performed with one-way ANOVA with Tukey's *post hoc* test. (*) $P < 0.05$. WT vs SMN(5): $P = 0.0103$, $q = 4.592$, df=21. **g**, Repetitive nerve stimulation at different frequencies from 0.1 to 50 Hz does not change the amplitude of the M-response recorded from the footpad of uninjected and either AAV9-GFP (5) or AAV9-SMN (5) treated WT mice at P300. The box-and-whiskers graph shows the median, interquartile range, minimum and maximum from the following number of animals: WT (0.1-10 Hz n = 8; 20-50 Hz n = 6); WT + AAV-GFP(5) (n = 8); WT + AAV-SMN(5) (0.1-10 Hz n = 8; 20 Hz n = 7; 50 Hz n = 6). Statistics were performed with one-way ANOVA with Tukey's *post hoc* test. (ns) no significance. WT: $P = 0.9938$, $F_{4, 31} = 0.05630$; WT + AAV-GFP(5): $P = 0.6199$, $F_{4, 35} = 0.06660$; WT + AAV-SMN(5): $P = 0.5344$, $F_{4, 32} = 0.07997$.

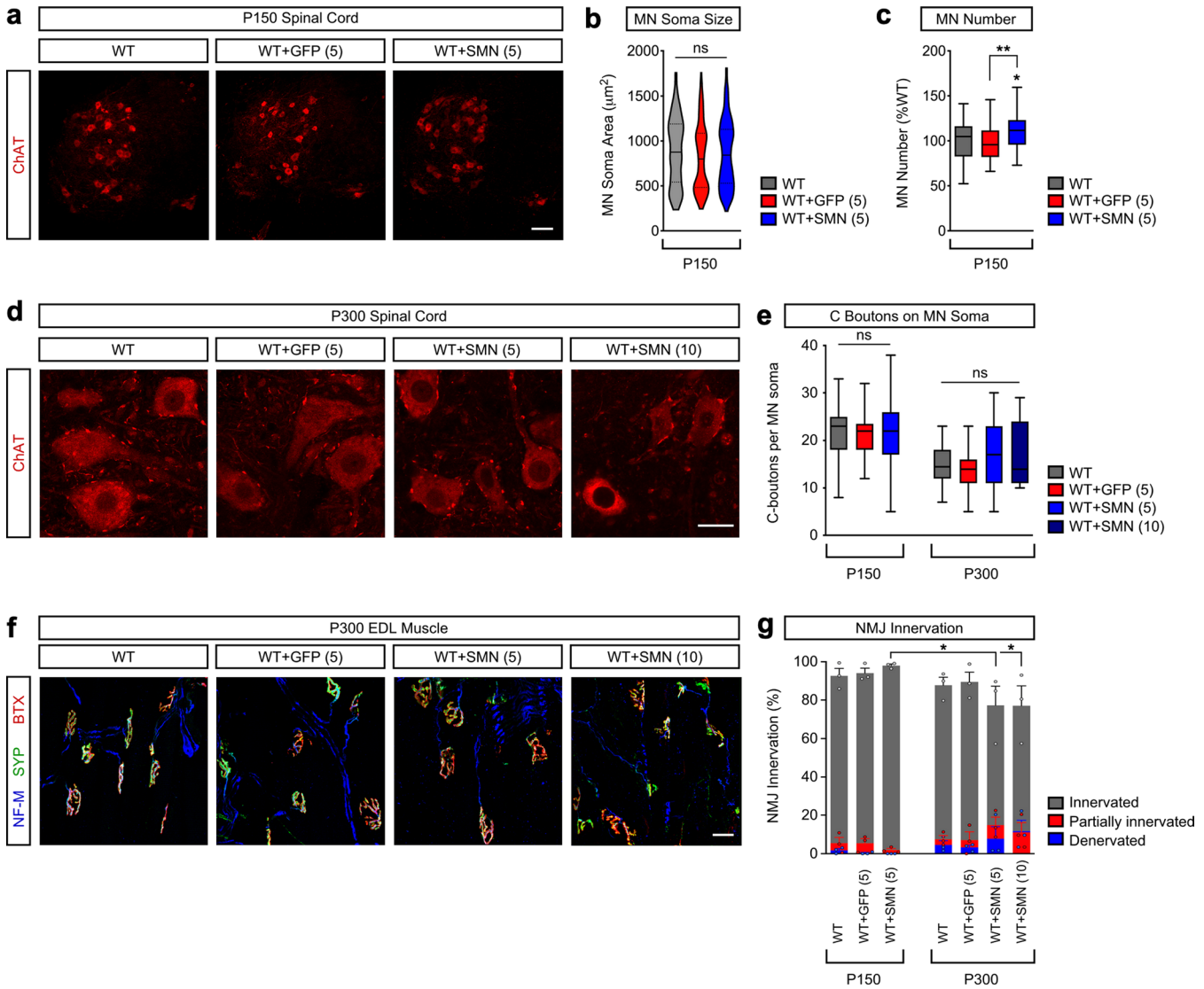


**Extended Data Fig. 2 | Effects of AAV9-SMN on motor neuron survival, C-boutons and NMJ innervation in WT mice. a**, ChAT immunostaining of L5 spinal segments from uninjected, AAV9-GFP (5) and AAV9-SMN (5) injected WT mice at P150. Scale bar=100 µm. **b**, Soma size of MNs from the same groups as in (**a**) at P150. The violin plot shows the median (solid line) and interquartile range (dotted lines) from the following number of MNs (WT, n = 227 neurons; WT + GFP(5), n = 234 neurons; WT + SMN(5), n = 234 neurons) from 3 animals per group. Statistics were performed with one-way ANOVA with Tukey's *post hoc* test. (ns) no significance. P = 0.3083, $F_{3, 449} = 1.180$. **c**, Percentage of the number of L5 LMC MNs per 75 µm section relative to WT in the same groups as in (**a**) at P150. The box-and-whiskers graph shows the median, interquartile range, minimum and maximum from the following number of sections (WT, n = 36 sections; WT + GFP(5), n = 31 sections; WT + SMN(5), n = 43 sections) from 3 animals per group. Statistics were performed with one-way ANOVA with Tukey's *post hoc* test. (*) $P < 0.05$; (**) $P < 0.01$. WT vs SMN(5): P = 0.0284, q = 3.678, df=107; GFP(5) vs SMN(5): P = 0.0064, q = 4.420, df=107. **d**, ChAT immunostaining of L5 LMC MNs from uninjected, AAV9-GFP (5) and AAV9-SMN (5 and 10) injected WT mice at P300. Scale bar=25 µm. **e**, Total number of ChAT$^+$ C-boutons on L5 LMC MNs from the same groups as in (**d**) at P150 and P300. The box-and-whiskers graph shows the median, interquartile range, minimum and maximum from the following numbers of neurons and animals at P150 (WT, n = 39 neurons, n = 3 animals; WT + GFP(5), n = 37 neurons, n = 3 animals; WT + SMN(5), n = 49 neurons, n = 3 animals) and P300 (WT, n = 28 neurons, n = 3 animals; WT + GFP(5), n = 31 neurons, n = 3 animals; WT + SMN(5), n = 36 neurons, n = 3 animals; WT + SMN(10), n = 14 neurons, n = 4 animals). Statistics were performed with one-way ANOVA with Tukey's *post hoc* test. (ns) no significance. For MNs at P150, P = 0.9855, $F_{2, 122} = 0.01456$. For MNs at P300, P = 0.0651, $F_{3, 105} = 2.481$. **f**, NMJ immunostaining of EDL muscles with Neurofilament-M (NF-M), Synaptophysin (SYP) and bungarotoxin (BTX) from the same groups as in (**a**) at P300. Scale bar=25 µm. **g**, Percentage of innervated, partially innervated and denervated NMJs in the EDL muscle from the same groups as in (**a**) at P150 and P300. Data represent mean and SEM (n = 3 animals). Statistics were performed with two-way ANOVA with Tukey's *post hoc* test. (*) $P < 0.05$. For innervated NMJs: SMN(5) P150 vs SMN(5) P300: P = 0.0346, q = 4.588, df=42; SMN(5) P150 vs SMN(10) P300: P = 0.0317, q = 4.636, df=42.

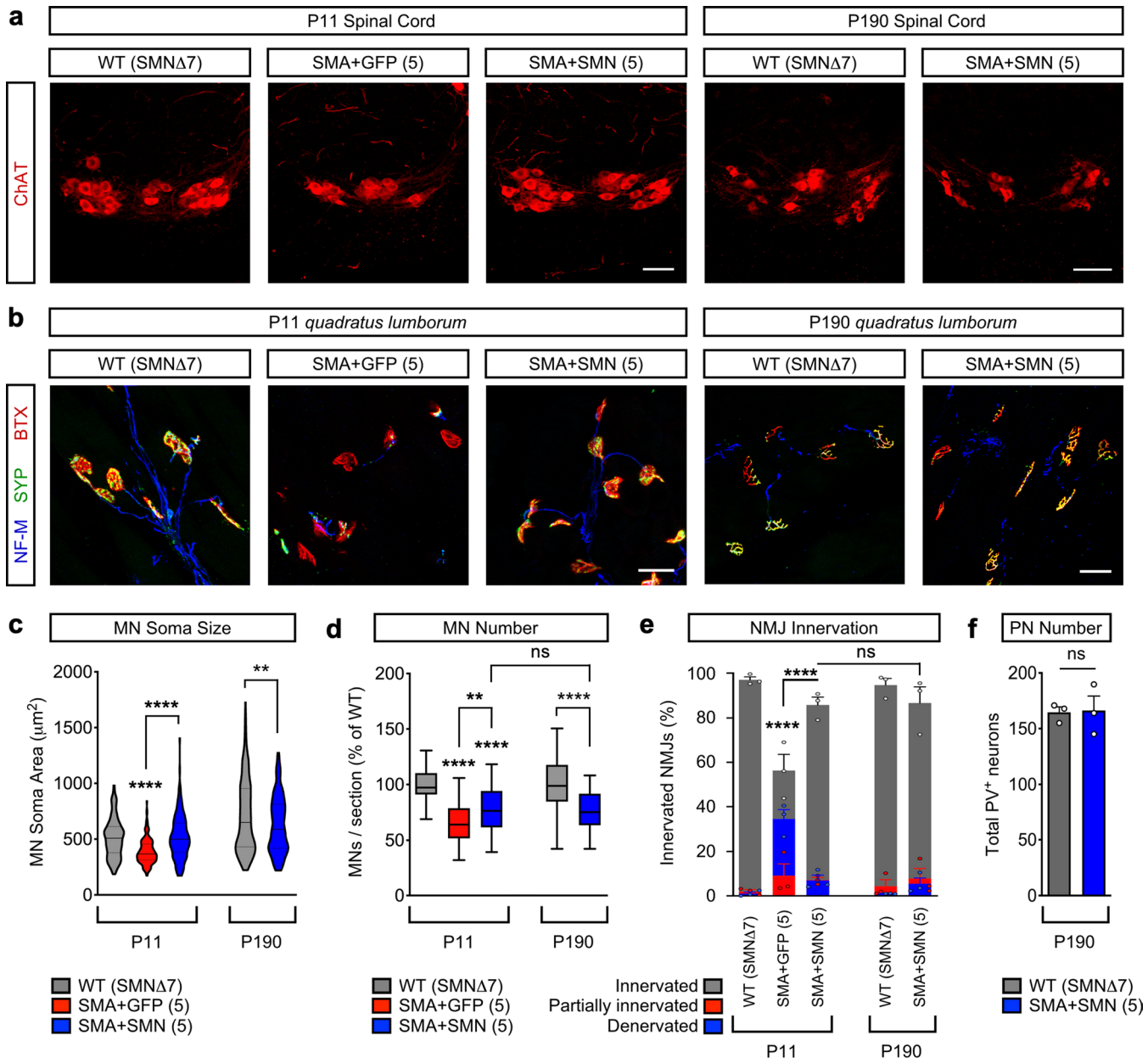


**Extended Data Fig. 3 | See next page for caption.**

**Extended Data Fig. 3 | Effects of AAV9-SMN on motor neuron survival, soma size and NMJ innervation in SMA mice. a**, ChAT immunostaining of L2 MNs from untreated WT (SMNΔ7) mice and either AAV9-GFP (5) or AAV9-SMN (5) treated SMA mice at the indicated times. Scale bars=75 μm (P11) and 100 μm (P190). **b**, NMJ immunostaining with Neurofilament-M (NF-M), Synaptophysin (SYP) and bungarotoxin (BTX) of QL muscles from the same groups as in (**a**). Scale bar=25 μm (P11) and 50 μm (P190). **c**, Soma size of MNs from the same groups as in (**a**) at P11 and P190. The violin plot shows the median (solid line) and interquartile range (dotted lines) from the following number of MNs at P11 (WT (SMNΔ7), n = 230 neurons; SMA + GFP(5), n = 185 neurons; SMA + SMN(5), n = 175 neurons) and P190 (WT (SMNΔ7), n = 231 neurons; SMA + SMN(5), n = 164 neurons) from 3 animals per group. Statistics were performed with one-way ANOVA with Tukey's *post hoc* test. (**) $P < 0.01$; (****) $P < 0.0001$. WT (SMNΔ7) P11 vs SMA + GFP(5) P11: $P < 0.0001$, $q = 7.696$, df=980; SMA + GFP(5) P11 vs SMA + SMN(5) P11: $P = < 0.0001$, $q = 7.714$, df=980; WT (SMNΔ7) P190 vs SMA + SMN(5) P190: $P = 0.0058$, $q = 4.841$, df=980. **d**, Percentage of the number of MNs per 75 μm section relative to WT (SMNΔ7) in the same groups as in (**a**) at P11 and P190. The box-and-whiskers graph shows the median, interquartile range, minimum and maximum from the following number of sections and animals at P11 (WT (SMNΔ7), n = 48 sections, n = 3 animals; SMA + GFP(5), n = 58 sections, n = 6 animals; SMA + SMN(5), n = 56 sections n = 6 animals) and P190 (WT (SMNΔ7), n = 42 sections, n = 3 animals; SMA + SMN(5), n = 41 sections, n = 3 animals). Statistics were performed with one-way ANOVA with Tukey's *post hoc* test. (**) $P < 0.01$; (***) $P < 0.001$; (ns) no significance. WT (SMNΔ7) P11 vs SMA + GFP(5) P11: $P < 0.0001$, $q = 13.58$, df=241; WT (SMNΔ7) P11 vs SMA + SMN(5) P11: $P < 0.0001$, $q = 8.359$, df=241; SMA + GFP(5) P11 vs SMA + SMN(5) P11: $P = 0.0018$, $q = 5.364$, df=241; WT (SMNΔ7) P190 vs SMA + SMN(5) P190: $P < 0.0001$, $q = 8.108$, df=241; SMA + SMN(5) P11 vs SMA + SMN(5) P190: $P = 0.9927$, $q = 0.6110$, df=241. **e**, Percentage of innervated, partially innervated and denervated NMJs relative to WT (SMNΔ7) in the QL muscle from the same groups as in (**b**) at P11 and P190. Data represent mean and SEM (n = 3 animals). Statistics were performed with two-way ANOVA with Tukey's *post hoc* test. (****) $P < 0.0001$; (ns) no significance. For innervated NMJs: WT (SMNΔ7) P11 vs SMA + GFP(5) P11: $P < 0.0001$, $q = 10.72$, df=30; SMA + GFP(5) P11 vs SMA + SMN(5) P11: $P < 0.0001$, $q = 7.789$, df=30; SMA + SMN(5) P11 vs SMA + SMN(5) P190: $P = 0.9999$, $q = 0.2233$, df=30. **f**, Total number of $PV^+$ PNs in L2 DRGs from untreated WT (SMNΔ7) mice and AAV9-SMN (5) treated SMA mice at P190. Data represent mean and SEM (n = 3 DRGs from n = 3 animals). Statistics were performed with unpaired Student's t-test. (ns) no significance. $P = 0.9106$, $t = 0.1196$, df=4.

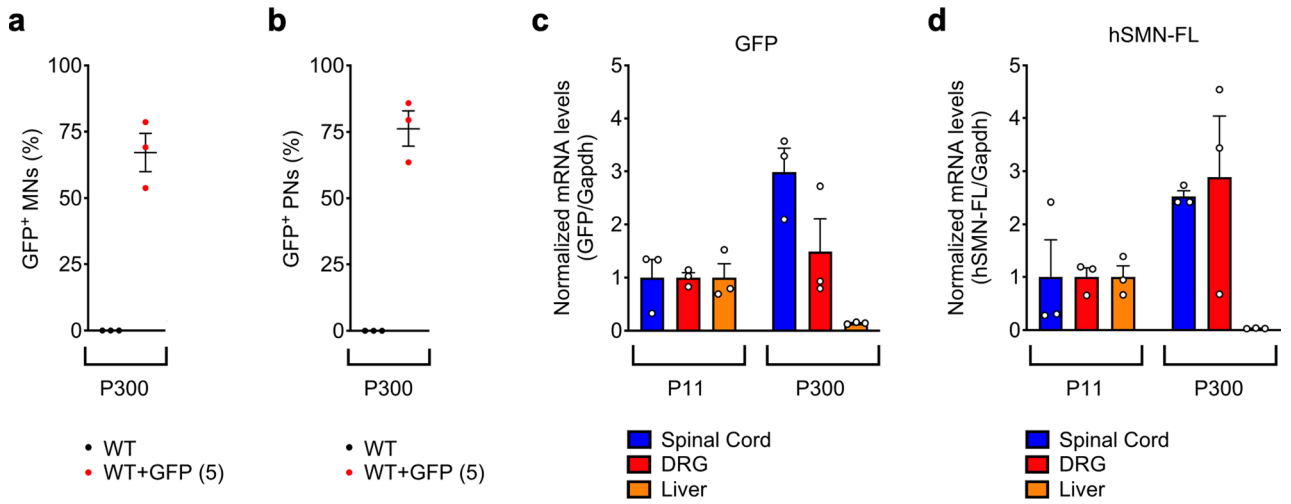


**Extended Data Fig. 4 | Efficiency of AAV9 transduction and long-term transgene expression in tissues of WT mice. a**, Percentage of GFP⁺ L5 LMC MNs from uninjected and AAV9-GFP (5) injected WT mice at P300. Data represent mean and SEM (n = 3 animals). **b**, Percentage of GFP⁺ PNs in L5 DRGs from the same groups as in (**a**) at P300. Data represent mean and SEM (n = 3 animals). **c**, RT-qPCR analysis of GFP mRNA in spinal cord, DRG and liver from WT mice injected with AAV9-GFP (5) at P11 and P300. Data represent mean and SEM (n = 3 animals) normalized to Gapdh mRNA and expressed relative to levels at P11 (set as 1). **d**, RT-qPCR analysis of full-length human SMN (hSMN-FL) mRNA in spinal cord, DRG and liver from WT mice injected with AAV9-SMN (5) at P11 and P300. Data represent mean and SEM (n = 3 animals) normalized to Gapdh mRNA and expressed relative to levels at P11 (set as 1).

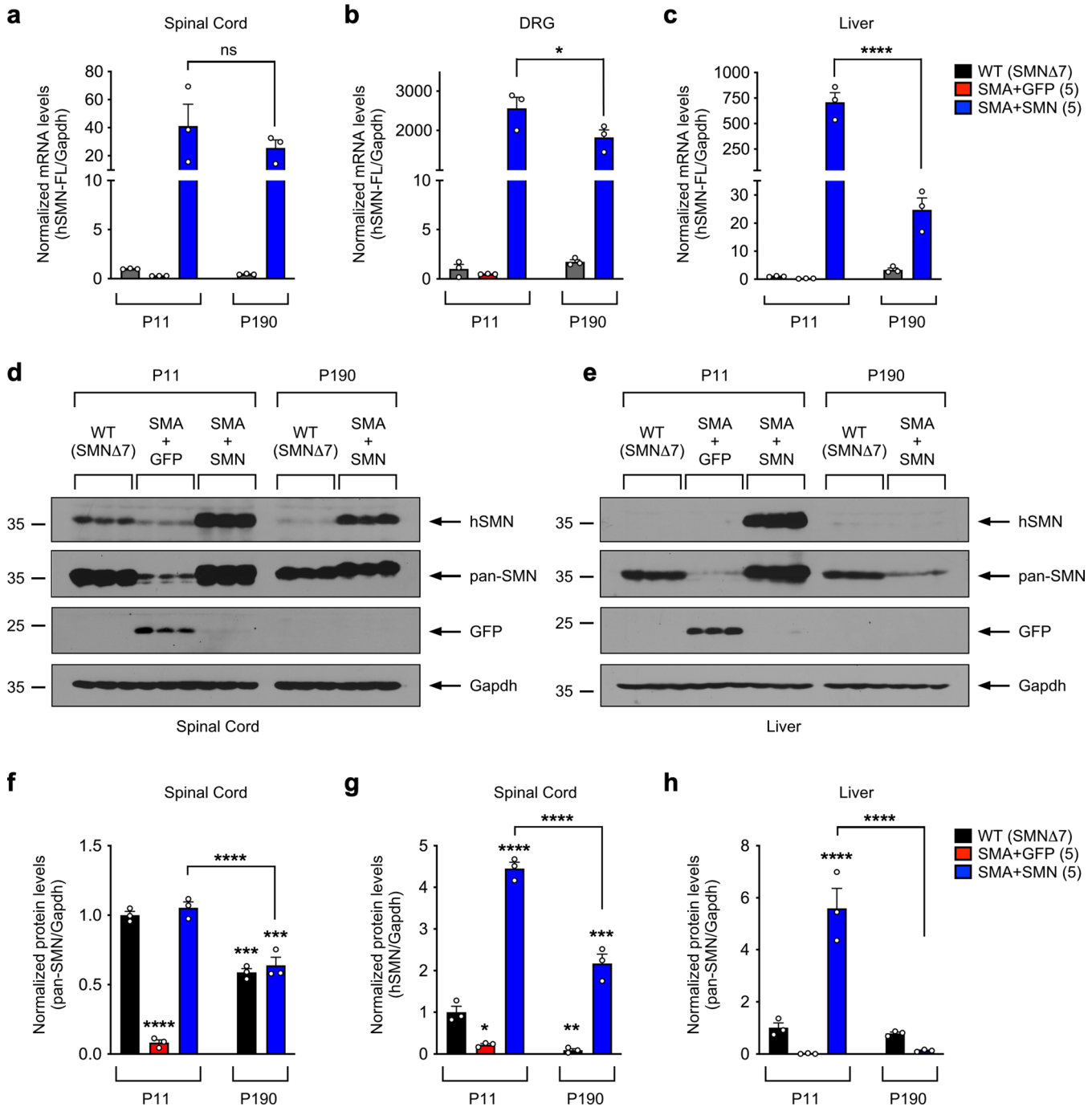


**Extended Data Fig. 5 | See next page for caption.**

**Extended Data Fig. 5 | AAV9-SMN leads to persistent SMN overexpression in the spinal cord and DRGs but not the liver of SMA mice. a-c**, RT-qPCR analysis of hSMN-FL mRNA levels in spinal cord (**a**), DRG (**b**) and liver (**c**) of uninjected WT (SMNΔ7) mice and SMA mice injected with either AAV9-GFP (5) or AAV9-SMN (5) at the indicated times. Data represent mean and SEM (n = 3 animals) normalized to Gapdh mRNA and expressed relative to levels in WT (SMNΔ7) mice (set as 1). Statistics were performed with one-way ANOVA with Tukey's *post hoc* test. (*) $P < 0.05$; (****) $P < 0.0001$; (ns) no significance. For spinal cord: SMA + SMN(5) P11 vs SMA + SMN(5) P190: $P = 0.5887$, $q = 2.111$, df=10. For DRG: SMA + SMN(5) P11 vs SMA + SMN(5) P190: $P = 0.0396$, $q = 4.866$, df=10. For liver: SMA + SMN(5) P11 vs SMA + SMN(5) P190: $P < 0.0001$, $q = 16.28$, df=10. **d-e**, Western blot analysis of spinal cord (**d**) and liver (**e**) from the same groups as in (**a**). SMN expression was analyzed with antibodies that specifically detect only human SMN (hSMN) or both human and mouse SMN (pan-SMN). Cropped images are shown. **f**, Quantification of total SMN protein levels from the Western blot analysis in (**d**). Data represent mean and SEM (n = 3 animals) normalized to Gapdh and expressed relative to levels in WT (SMNΔ7) mice (set as 1). Statistics were performed with one-way ANOVA with Tukey's *post hoc* test. (****) $P < 0.0001$; (***) $P < 0.001$. WT (SMNΔ7) P11 vs SMA + GFP(5) P11: $P < 0.0001$, $q = 24.80$, df=10; WT (SMNΔ7) P11 vs WT (SMNΔ7) P190: $P = 0.0001$, $q = 11.12$, df=10; WT (SMNΔ7) P11 vs SMA + SMN(5) P190: $P = 0.0003$, $q = 9.975$, df=10; SMA + SMN(5) P11 vs SMA + SMN(5) P190: $P < 0.0001$, $q = 11.23$, df=10. **g**, Quantification of human SMN protein levels from the Western blot analysis in (**d**). Data represent mean and SEM (n = 3 animals) normalized to Gapdh and expressed relative to levels in WT (SMNΔ7) mice (set as 1). Statistics were performed with one-way ANOVA with Tukey's *post hoc* test. (****) $P < 0.0001$; (***) $P < 0.001$; (**) $P < 0.01$; (*) $P < 0.05$. WT (SMNΔ7) P11 vs SMA + GFP(5) P11: $P = 0.0165$, $q = 5.671$, df=10; WT (SMNΔ7) P11 vs SMN(5) P11: $P < 0.0001$, $q = 25.08$, df=10; WT (SMNΔ7) P11 vs SMA + SMN(5) P190: $P = 0.0009$, $q = 8.513$, df=10. SMA + SMN(5) P11 vs SMA + SMN(5) P190: $P < 0.0001$, $q = 16.57$, df=10. **h**, Quantification of total SMN protein levels from the Western blot analysis in (**e**). Data represent mean and SEM (n = 3 animals) normalized to Gapdh and expressed relative to levels in WT (SMNΔ7) mice (set as 1). Statistics were performed with one-way ANOVA with Tukey's *post hoc* test. (****) $P < 0.0001$. WT (SMNΔ7) P11 vs SMA + SMN(5) P11: $P < 0.0001$, $q = 13.08$, df=10; SMA + SMN(5) P11 vs SMA + SMN(5) P190: $P < 0.0001$, $q = 15.56$, df=10.

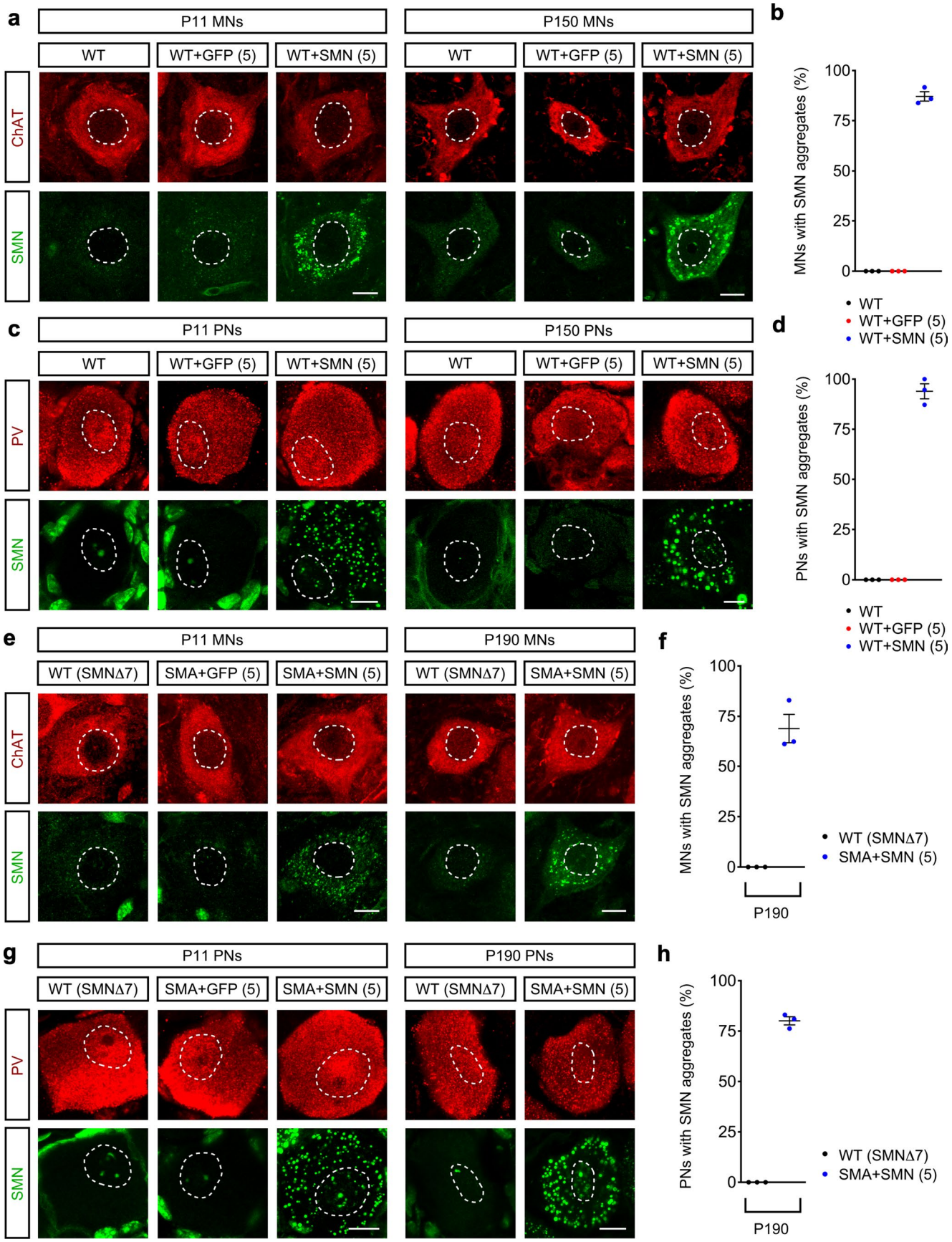


**Extended Data Fig. 6 | See next page for caption.**

**Extended Data Fig. 6 | AAV9-SMN drives cytoplasmic aggregation of overexpressed SMN in motor circuit neurons of mouse models. a**, ChAT and SMN immunostaining of L5 LMC MNs from uninjected and either AAV9-GFP (5) or AAV9-SMN (5) injected WT mice at P11 and P150. Scale bar=10 μm. **b**, Percentage of L5 LMC MNs with SMN aggregates in the same groups as in (**a**) at P300. Data represent mean and SEM (n = 3 animals). **c**, PV and SMN immunostaining of L5 DRG PNs from uninjected and either AAV9-GFP (5) or AAV9-SMN (5) injected WT mice at P11 and P150. Scale bar=10 μm. **d**, Percentage of L5 DRG PNs with SMN aggregates in the same groups as in (**c**) at P300. Data represent mean and SEM (n = 3 animals). **e**, ChAT and SMN immunostaining of L2 MNs from WT (SMNΔ7) mice and either AAV9-GFP (5) or AAV9-SMN (5) injected SMA mice at the indicated time points. Scale bar=10 μm. **f**, Percentage of L2 MNs with SMN aggregates in the same groups as in (**e**) at P190. Data represent mean and SEM (n = 3 animals). **g**, PV and SMN immunostaining of L2 DRG PNs from the same groups as in (**e**). Scale bar=10 μm. **h**, Percentage of L2 PNs with SMN aggregates in the same groups as in (**g**) at P190. Data represent mean and SEM (n = 3 animals).

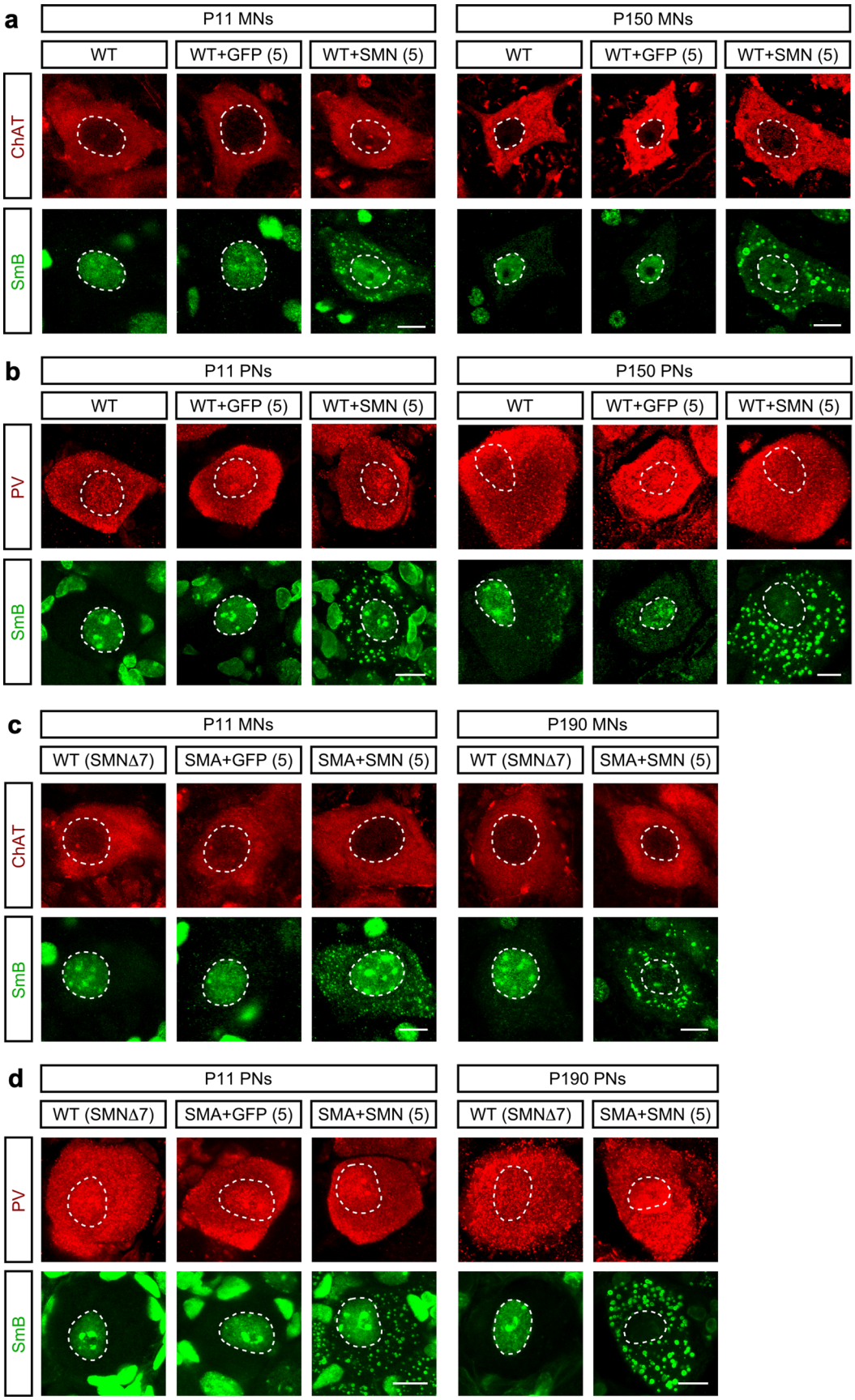


**Extended Data Fig. 7 | See next page for caption.**

**Extended Data Fig. 7 | AAV9-mediated SMN overexpression induces cytoplasmic aggregation of SmB in motor circuit neurons of mouse models.** **a**, ChAT and SmB immunostaining of L5 LMC MNs from uninjected and either AAV9-GFP (5) or AAV9-SMN (5) injected WT mice at P11 and P150. Scale bar=10 μm. **b**, PV and SmB immunostaining of L5 DRG PNs from the same groups as in (**a**). Scale bar=10 μm. **c**, ChAT and SmB immunostaining of L2 MNs from WT (SMNΔ7) mice and either AAV9-GFP (5) or AAV9-SMN (5) injected SMA mice at the indicated time points. Scale bar=10 μm. **d**, PV and SmB immunostaining of L2 PNs from the same groups as in (**c**). Scale bar=10 μm.

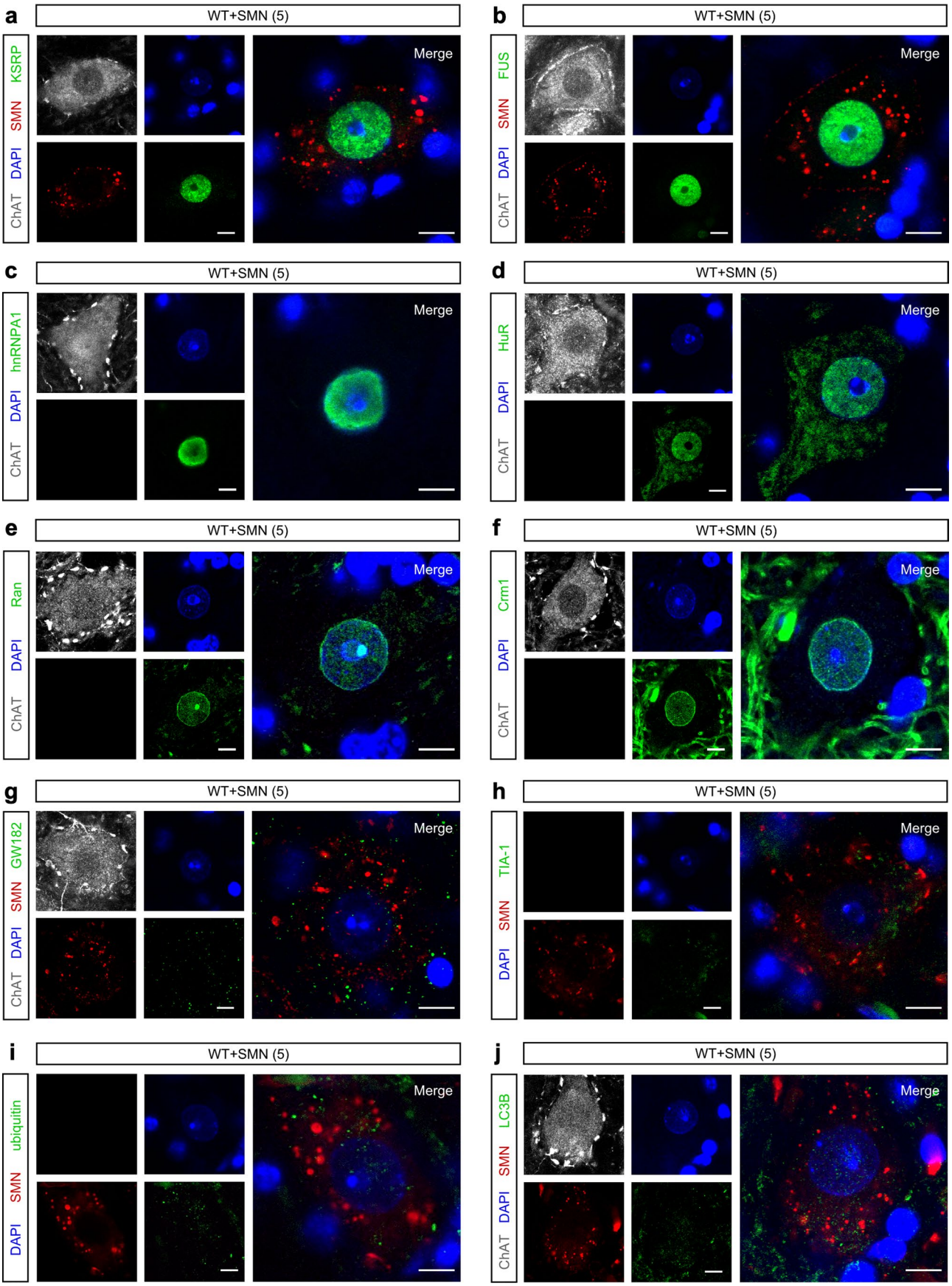


**Extended Data Fig. 8 | See next page for caption.**

**Extended Data Fig. 8 | Immunohistochemical analysis of cytoplasmic SMN aggregates in motor neurons. a-d**, Immunostaining of L5 LMC MNs from WT mice injected with AAV9-SMN (5) at P300 with DAPI, ChAT, SMN and RNA-binding proteins KSRP (**a**), FUS (**b**), hnRNPA1 (**c**) or HuR (**d**) as indicated. Scale bar=5 μm. **e-f**, Immunostaining with DAPI, ChAT and RNA transport factors Ran (**e**) and Crm1 (**f**) in the same MNs as in (**a**). Scale bar=5 μm. **g-h**, Immunostaining with DAPI, ChAT, SMN and either GW182 to label P-bodies (**g**) or TIA-1 to label stress granules (**h**) in the same MNs as in (**a**). Scale bar=5 μm. **i-j**, Immunostaining with DAPI, ChAT, SMN and either ubiquitin (**i**) or the autophagy marker LC3B (**j**) in the same MNs as in (**a**). Scale bar=5 μm.

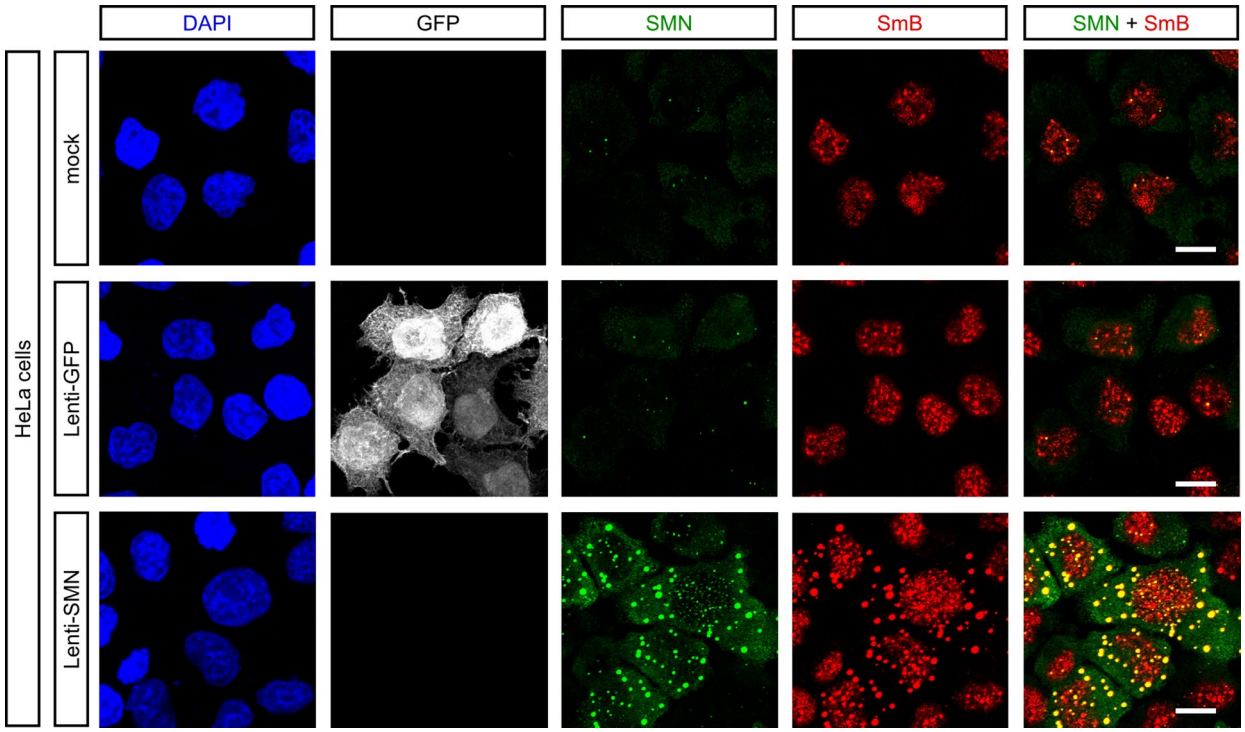


**Extended Data Fig. 9 | Viral-mediated overexpression of human SMN induces cytoplasmic aggregation and sequestration of SmB in human cells.** HeLa cells were untreated (mock) or transduced with lentivirus expressing either GFP (Lenti-GFP) or human SMN (Lenti-SMN). Immunostaining with DAPI, GFP, SMN and SmB was performed five days post transduction. Scale bar=10 μm.

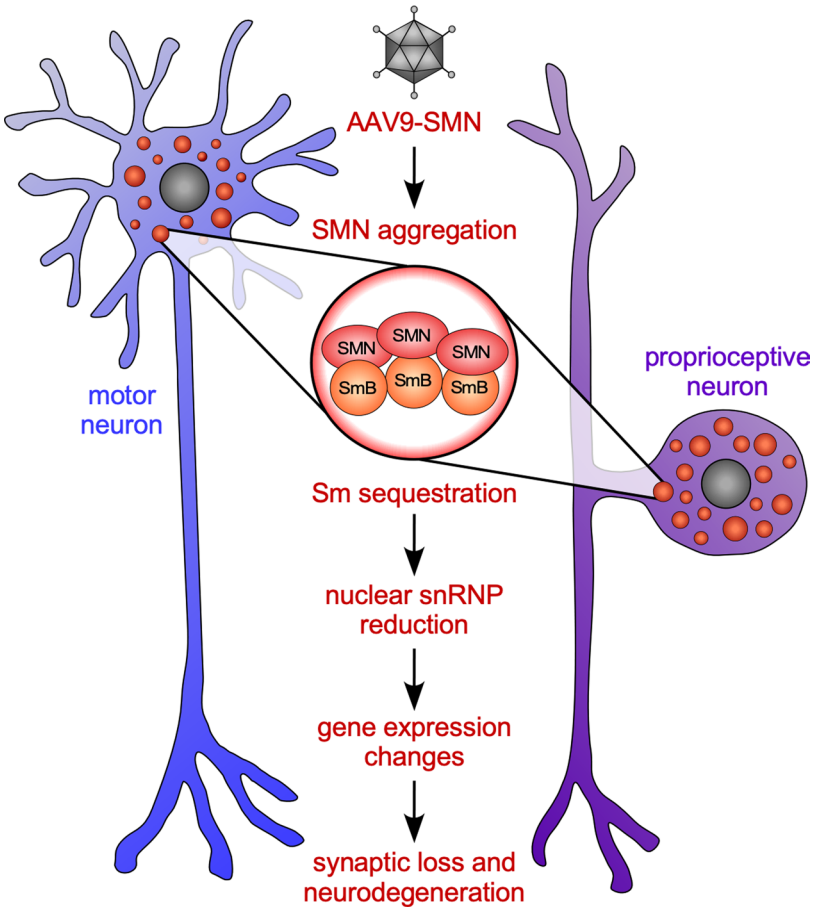


**Extended Data Fig. 10 | Model of the toxic effects of long-term AAV9-mediated SMN overexpression in neurons.** Schematic depicting the gain of toxic function mechanisms induced by long-term overexpression of SMN in the sensory-motor circuit of mouse models (see text for further details).

nature research

Corresponding author(s): Livio Pellizzoni

Last updated by author(s): Feb 10, 2021

# Reporting Summary

Nature Research wishes to improve the reproducibility of the work that we publish. This form provides structure for consistency and transparency in reporting. For further information on Nature Research policies, see our Editorial Policies and the Editorial Policy Checklist.

## Statistics

For all statistical analyses, confirm that the following items are present in the figure legend, table legend, main text, or Methods section.

| n/a | Confirmed | |
|---|---|---|
| ☐ | ☒ | The exact sample size (*n*) for each experimental group/condition, given as a discrete number and unit of measurement |
| ☐ | ☒ | A statement on whether measurements were taken from distinct samples or whether the same sample was measured repeatedly |
| ☐ | ☒ | The statistical test(s) used AND whether they are one- or two-sided<br>*Only common tests should be described solely by name; describe more complex techniques in the Methods section.* |
| ☐ | ☒ | A description of all covariates tested |
| ☐ | ☒ | A description of any assumptions or corrections, such as tests of normality and adjustment for multiple comparisons |
| ☐ | ☒ | A full description of the statistical parameters including central tendency (e.g. means) or other basic estimates (e.g. regression coefficient) AND variation (e.g. standard deviation) or associated estimates of uncertainty (e.g. confidence intervals) |
| ☐ | ☒ | For null hypothesis testing, the test statistic (e.g. *F*, *t*, *r*) with confidence intervals, effect sizes, degrees of freedom and *P* value noted<br>*Give P values as exact values whenever suitable.* |
| ☒ | ☐ | For Bayesian analysis, information on the choice of priors and Markov chain Monte Carlo settings |
| ☒ | ☐ | For hierarchical and complex designs, identification of the appropriate level for tests and full reporting of outcomes |
| ☒ | ☐ | Estimates of effect sizes (e.g. Cohen's *d*, Pearson's *r*), indicating how they were calculated |

*Our web collection on statistics for biologists contains articles on many of the points above.*

## Software and code

Policy information about availability of computer code

| | |
|---|---|
| Data collection | Clampex (v10.2, Molecular Devices) (for acquisition of physiology recordings); LEICA LAS AF software (v2.5.2.6939) (for confocal image acquisition). |
| Data analysis | Clampfit (v10.2, Molecular Devices) (for off-line analysis of physiology recording); LEICA LAS X (v1.9.0.13747) and Fiji (v1.0) (for image quantification); GraphPad Prism (v8.4.2) (for graphing and statistical analysis); RTA3 and bcl2fastq2 (v2.20) (for base calling and conversion of RNASeq data); OLego (v1.1.5) and Quantas (for mapping and quantitative analysis of RNASeq data); DAVID v6.8 (for gene ontology anaysis). |

For manuscripts utilizing custom algorithms or software that are central to the research but not yet described in published literature, software must be made available to editors and reviewers. We strongly encourage code deposition in a community repository (e.g. GitHub). See the Nature Research guidelines for submitting code & software for further information.

## Data

Policy information about availability of data

All manuscripts must include a data availability statement. This statement should provide the following information, where applicable:

- Accession codes, unique identifiers, or web links for publicly available datasets
- A list of figures that have associated raw data
- A description of any restrictions on data availability

The data supporting the findings of this study are available in this paper or the Supplementary Information. Sequencing data have been deposited in the GEO database under accession number GSE149391. Full uncropped blots are available as Source data. Any other raw data that support the findings of this study are available from the corresponding author upon reasonable request.

# Field-specific reporting

Please select the one below that is the best fit for your research. If you are not sure, read the appropriate sections before making your selection.

☒ Life sciences ☐ Behavioural & social sciences ☐ Ecological, evolutionary & environmental sciences

For a reference copy of the document with all sections, see nature.com/documents/nr-reporting-summary-flat.pdf

# Life sciences study design

All studies must disclose on these points even when the disclosure is negative.

| | |
|---|---|
| Sample size | Sample sizes were based on our previously published work in the field in order to support meaningful conclusions (PMID: 31851921, PMID: 30012555, PMID: 29281826, PMID: 28504671, PMID: 21315257). The sample size for each experiment is detailed in the figure legends. No statistical methods were used to predetermine sample size. |
| Data exclusions | No data was excluded from the analysis. |
| Replication | All the data in the manuscript were generated using at least three independent biological replicates. |
| Randomization | Experimental animals were randomly assigned to treatment groups. No other experiments required randomization. |
| Blinding | Blinding to treatment conditions was utilized when running behavioral assays, sequencing experiments, and electrophysiological recordings. |

# Reporting for specific materials, systems and methods

We require information from authors about some types of materials, experimental systems and methods used in many studies. Here, indicate whether each material, system or method listed is relevant to your study. If you are not sure if a list item applies to your research, read the appropriate section before selecting a response.

## Materials & experimental systems

| n/a | Involved in the study |
|---|---|
| ☐ | ☒ Antibodies |
| ☐ | ☒ Eukaryotic cell lines |
| ☒ | ☐ Palaeontology and archaeology |
| ☐ | ☒ Animals and other organisms |
| ☒ | ☐ Human research participants |
| ☒ | ☐ Clinical data |
| ☒ | ☐ Dual use research of concern |

## Methods

| n/a | Involved in the study |
|---|---|
| ☒ | ☐ ChIP-seq |
| ☒ | ☐ Flow cytometry |
| ☒ | ☐ MRI-based neuroimaging |

# Antibodies

Antibodies used

Primary Antibodies:
SMN, Mouse, 1:100 (IHC), 1:10,000 (WB) (BD - 610646); hSMN exon 7, Rabbit, 1:250 (custom, see PMID:9845364); Gapdh, Mouse, 1:5000 (Millipore Sigma MAB374), SmB, Mouse, 1:2 (IHC), (custom, see PMID: 17023415); GFP, Rabbit, 1:5000 (WB) (Sigma - G1544); ChAT, Goat, 1:100 (Millipore - AB144P); Parvalbumin, Chicken, 1:10000 (Covance, custom, see PMID:28504671 ); Parvalbumin, Rabbit, 1:1000 (Swant - PV27); GFP, Chicken, 1:500 (IHC) (Aves - GFP-1020); VGluT1, Guinea pig, 1:5000 (Covance, see PMID:28504671); Synaptophysin, Guinea pig, 1:500 (Synaptic Systems - 101-004); Neurofilament-M, Rabbit, 1:1000 (Millipore - AB1987); Bungarotoxin, 1:500 (Invitrogen - T1175); GW182, Rabbit, 1:200 (Bethyl - A302-330A); LC3B, Rabbit, 1:200 (Novus - NB600-1384); FUS, Rabbit, 1:1000 (Bethyl - A300-A293); KSRP, Rabbit, 1:100 (Bethyl - 021A-1); HuR, Rabbit, 1:200 (Santa Cruz - sc-5261); hnRNPA1, Mouse, 1:100 (Santa Cruz - sc-32301); Crm1, Mouse, 1:200 (BD - 611832); Ran, Mouse, 1:200 (BD - 610340); TIA-1, Goat, 1:200 (Santa Cruz - sc-1751); Ubiquitin, Goat, 1:100 (Santa Cruz - sc-6085); DAPI, 1:1000 (Molecular Probes - D3571)

Secondary Antibodies:
488 anti-rabbit, Donkey, 1:250 (Jackson 711-545-152), 488 anti-goat, Donkey, 1:250 (Jackson 705-545-147), 488 anti-chicken, Donkey, 1:250 (Jackson 703-545-155), 488 anti-mouse IgG1, Goat 1:250 (Jackson 115-545-205), Cy3 anti-rabbit, Donkey, 1:250 (Jackson 711-165-152), Cy3 anti-mouse, Donkey, 1:250 (Jackson 715-165-150), Cy3 anti-goat, Donkey, 1:250 (Jackson 705-165-147), Cy3 anti-mouse IgG1, Goat 1:250 (Jackson 115-165-205), Cy3 anti-mouse IgG2a, Goat 1:250 (Jackson 115-165-206), Cy5 anti-goat, Donkey, 1:250 (Jackson 705-175-147), Cy5 anti-guinea pig, Donkey 1:250 (Jackson 706-175-148), Cy5 anti-chicken, Donkey 1:250 (Jackson 703-175-155), Fab anti-mouse IgG, Donkey 1:250 (Jackson 715-007-003), HRP anti-mouse, Goat 1:10000 (Jackson 115-035-044), HRP anti-rabbit, Goat 1:10000 (Jackson 111-035-003).

Validation

The antibodies used in this study have been widely published and experimentally validated as described below. Some manufacturers statements were taken from their respective websites, in which further information and references are available. In-house testing

included validation of the correct performance of antibodies through detection of a single specific band at the expected molecular weight by western blotting. In several instances, the specificity of the antibodies has been further validated in cells/mice lacking the targeted protein by western blotting and/or immunofluorescence/immunohistochemistry experiments.

The SMN antibody (clone 8, BD) has been previously validated in WT and SMN-deficient cells and tissue (PMID: 17895963; PMID: 23063131; PMID: 23967270; PMID: 24332368; PMID: 30012555).

The SmB antibody has been previously validated in WT and SmB-deficient cells and tissue (PMID: 17023415; PMID: 17895963; PMID: 22037760; PMID: 26063904; PMID: 30012555; PMID: 31570875).

The hSMN exon 7 antibody is an afffinity purified rabbit polyclonal raised against the amino acid sequence encoded by exon 7 of human SMN and was previously validated (PMID: 9845364).

The Gapdh antibody, clone 6C5 is a well published and extensively characterized monoclonal antibody. This purified mAb detects Glyceraldehyde-3-Phosphate Dehydrogenase (GAPDH) and has been published and validated for use in ELISA, IP, IC, IF, IH & WB with species reactivity in rabbit, feline, mouse, rat, fish, pig, canine and human (Millipore Sigma) (PMID: 22037760).

The anti-GFP, N-Terminal is produced in rabbit and reacts specifically with GFP fusion proteins. It has been validated for applications including immunoblotting and immunoprecipitation (Sigma) (PMID:31851921).

Anti-Choline Acetyltransferase Antibody detects ChAT in mouse, rabbit, and human and has been published and validated for use in IH(P), IC, IH and WB (Millipore) (PMID:31851921, PMID:28504671, PMID:30012555, PMID:29281826).

The specificity of the anti-Parvalbumin chicken antibody has been previously validated for use in IHC (PMID: 28504671).

The specificity of the anti-Parvalbumin rabbit antibody has been validated in knock-out mice (Swant) and has reactivity with rat, mouse and human. It has been validated for use in immunohistochemistry and for immunoblotting (PMID:28384468).

The chicken GFP antibody has been previously validated for specificity and use in immunohistochemistry, Western blotting and ELISA (PMID: 29281826).

The VGluT1 antibodies were previously tested and reported in VGluT1 knock out tissues and validated for use in immunohistochemistry for mouse tissue (PMID:31851921, PMID:28504671, PMID:30012555, PMID:29281826).

The Synaptophysin antibody is specific for synaptophysin 1, and shows no cross-reactivity to other synaptophysins. It has reactivity agains human, rat, mouse, hamster, cow, chicken and frog and has been validated for application in Western blotting, immunoprecipitation and immunohistochemistry (Synaptic Systems) (PMID:31851921, PMID:28504671, PMID:30012555, PMID:29281826).

The Anti-Neurofilament M Antibody, C-terminus detects Neurofilament M (145 kDa) in human, mouse, rabbit, bovine, chicken, pig, rat, quail and reptile and has been published and validated for use in IC, IH, IH(P) & WB (Millipore) (PMID:31851921, PMID:28504671, PMID:30012555, PMID:29281826).

α-Bungarotoxin is an amino acid peptide extracted from Bungarus multicinctus venom, which binds with high affinity to the α-subunit of the nicotinic acetylcholine receptor (AChR). It has been validated to stain AChR in mouse skeletal muscle (Invitrogen) (PMID:31851921, PMID:28504671, PMID:30012555, PMID:29281826).

The GW182 antibody has been validated by the manufacturer and has species reactivity against human and mouse and has been used for immunofluorescence and Western blot (Bethyl) (PMID:21984184, PMID:23019594).

The LC3B antibody has been validated by the manufacturer by Western blot and published for other uses including immunohistochemistry, immunoprecipitation, and ELISA. Reactivity has been reported for mouse, zebrafish, canin, and primates (Novus) (PMID:31851921, PMID:24928515, PMID:18259115, PMID:25383539).

The FUS antibody has been validated by the manufacturer for use in immunohistochemistry, Western blot, and immunoprecipitation with species reactivity against human and mouse (Bethyl) (PMID:30021151, PMID:30044993).

The KSRP antibody has been validated by the manufacturer for use in immunohistochemistry, immunoprecipitation and Western blotting of human or mouse samples (Bethyl) (PMID:31296853, PMID:29771377).

The HuR antibody has been validated by the manufacturer for use in immunohistochemistry, immunoprecipitation, Western blotting and ELISA and can be used for detection in mouse, rat, human and Xenopus laevis samples (Santa Cruz) (PMID:30449617, PMID:24892821).

The hnRNPA1 antibody has been validated by the manufacturer for use in immunohistochemistry, Western blotting, immunoprecipitation and ELISA with species reactivity for mouse rat and human (Santa Cruz) (PMID:30220511, PMID:31251911, PMID:28431233).

The Crm1 antibody validation was performed by the manufacturer. This antibody is routinely tested by Western blot analysis at BD Biosciences Pharmingen and has also been validate for use in immunofluorescence. It has reactivity against human, mouse, rat, dog, and chicken (BD) (PMID:12192051).

The Ran antibody is routinely tested by the manufacturer for Western blot analysis and was validated for immunohistochemistry and immunoprecipitation. It has reactivity against human, mouse, rat, dog and chicken (BD) (PMID:29196813).

The TIA-1 antibody was validated by the manufacturer for detection in mouse, rat and human samples by Western blotting,

immunoprecipitation, immunofluorescence, immunohistochemistry and ELISA (Santa Cruz) (PMID:21189287, PMID:10938105). The ubiquitin antibody has been validated by the manufacturer for use in Western blotting, immunostaining and ELISA with reactivity against broad mammalian species (Santa Cruz) (PMID:21857683, PMID:29712835).

## Eukaryotic cell lines

Policy information about cell lines

| | |
|---|---|
| Cell line source(s) | HEK293T (Thermo Scientific Cat #HCL4517); HeLa S3 (ATCC CCL-2.2) |
| Authentication | The cell lines were not authenticated. |
| Mycoplasma contamination | The cell lines were not tested by mycoplasma contamination. |
| Commonly misidentified lines (See ICLAC register) | No commonly misidentified cell lines were used in this study. |

## Animals and other organisms

Policy information about studies involving animals; ARRIVE guidelines recommended for reporting animal research

| | |
|---|---|
| Laboratory animals | C57BL6J mice were obtained from the Jackson Laboratory (Jax stock #000664). The SMNΔ7 mouse line (Smn+/–/SMN2+/+/SMNΔ7+/+) used in this study to generate SMA mice was on a pure FVB background and was obtained from the Jackson Laboratory (Jax stock #005025). C57BL6J mice were used for experiments up to P300 and exact ages for each experiment are specified in the figure legends. SMNΔ7 mice were used for experiments up to P561 and exact ages for each experiment are specified in the figure legends. Experiments with C57BL6J and SMNΔ7 mice were performed with equal proportions of mice of both sexes and aggregated data are presented because gender-specific differences were not found. Mice were housed in a humidity (40-60%) and temperature (18-23 C) controlled animal facility with a 12 h/12 h light/dark cycle with free access to food and water. |
| Wild animals | This study did not involve wild animals. |
| Field-collected samples | This study did not involve samples collected from the field. |
| Ethics oversight | All mouse work was performed in accordance with the National Institutes of Health Guidelines on the Care and Use of Animals, complied with all ethical regulations and was approved by the IACUC committee of Columbia University. |

Note that full information on the approval of the study protocol must also be provided in the manuscript.